previously produced and analyzed knockout mice lacking MTH1 or ITPA. *Mth1*$^{-/-}$ mice are viable and survive normally but exhibit an increased incidence of spontaneous tumorigenesis in the liver, stomach and lung (8), while *Itpa*$^{-/-}$ mice die before weaning with features of growth retardation and heart failure (6).

ATP, the most abundant of the nucleotides, plays a fundamental role in a wide variety of cellular processes, including energy transfer, signal transduction, RNA synthesis, cytoskeleton remodeling and muscle contraction. Deamination of adenine at C-6 converts ATP to ITP; such modification is catalyzed by enzymes such as adenosine or AMP deaminase (9), or induced chemically under oxidative stress (7). Because ITP retains a molecular structure similar to that of ATP, it can act as an aberrant substrate replacing ATP in some biological processes (10,11). In the case of cardiac function, a number of sarcomere proteins require ATP for their normal activities. It is likely that during cardiac development in *Itpa*$^{-/-}$ mice the accumulated ITP competes with ATP, which is required for actomyosin function in the sarcomere, thus causing heart failure (6).

Bradshaw and Kuzminov (12) reported that an *Escherichia coli* mutant of *rdgB* gene-encoding inosine triphosphatase has no obvious phenotype; however, the mutant exhibits synergistic lethality in the presence of *recA* or *recBC* mutations. They concluded that RdgB acts to avoid incorporation of 2′-deoxyinosine (dI) in DNA and thereby blocks chromosome fragmentation by hydrolyzing dITP in *E. coli*. These observations strongly suggest that ITPA deficiency in mouse cells also causes chromosomal abnormalities.

In the present study, we examined mouse embryonic fibroblasts (MEFs) prepared from wild-type (*Itpa*$^{+/+}$), *Itpa*$^{+/-}$ and *Itpa*$^{-/-}$ embryos to explore the cellular dysfunction caused by ITPA deficiency. We found that *Itpa*$^{-/-}$ embryos accumulated more than eight times higher levels of dI in nuclear DNA than did wild-type embryos. Moreover, *Itpa*$^{-/-}$ primary MEFs with no ITP-hydrolyzing activity exhibited prolonged doubling times, increased chromosome aberrations and accumulation of single-strand breaks in nuclear DNA. Surprisingly, these phenotypes all disappeared following immortalization of *Itpa*$^{-/-}$ MEFs, with a significant increase in IDP-hydrolyzing activity accompanied by a decreased accumulation of dI in nuclear DNA. We have thus identified a novel enzyme which constitutes a dual enzyme system for eliminating dITP/ITP and dIDP/IDP from nucleotide pools together with ITPA in mammals.

MATERIALS AND METHODS

Nucleotides

Nucleotides used as substrates for enzyme assay were purchased from Sigma-Aldrich (St Louis, MO, USA), or Jena Bioscience GmbH (Jena, Germany). Separation and purification of nucleotides were performed on a Waters Alliance 2690 HPLC separation module (Waters Corp., Milford, MA, USA) equipped with a Model 996 photodiode array detector and a Wakopak Handy ODS column (4.6 × 250 mm) using 100 mM triethyl ammonium hydrogen carbonate solution (pH 7.4) (Wako Pure Chemicals, Osaka, Japan) as the mobile phase. Purified nucleotides were lyophilized five times with solubilization in distilled water.

Itpa gene knockout mice

Itpa gene knockout mice were established as described (6). Genotypes were analyzed using tail DNA. PCR primers used to detect the wild-type and *Itpa* mutant alleles were P46 and P47, or P29 and LNEO1, respectively (Supplementary Table S2). Heterozygous male (*Itpa*$^{+/-}$) were backcrossed with C57BL/6J female (*Itpa*$^{+/+}$) (Clea Japan, Tokyo, Japan) for more than five generations ($N > 5$). All animals were maintained in an air-conditioned, light/time-controlled, specific-pathogen-free room. All studies were approved by the Animal Care and Use Committee, Medical Institute of Bioregulation, Kyushu University.

Preparation of primary and immortalized MEFs

Twenty embryonic gestation day (E)13.5 and E14.5 embryos were obtained by intercross mating of inbred N10 or N11 *Itpa*$^{+/-}$ mice (three pairs). Their genotypes were *Itpa*$^{+/+}$, *Itpa*$^{+/-}$ and *Itpa*$^{-/-}$ at a ratio of 5:10:5. Skin fibroblasts were aseptically isolated from these embryos and at least four independent embryos were used for each genotype (*Itpa*$^{+/+}$, *Itpa*$^{+/-}$, *Itpa*$^{-/-}$). These primary MEFs were cultured in Dulbecco's Modified Eagle's Medium (DMEM) supplemented with 10% heat-inactivated fetal bovine serum (FBS), 100 units/ml penicillin and 100 μg/ml streptomycin at 37°C under 5% CO_2 in air. Primary MEFs in culture were harvested by treatment with 0.15% trypsin–0.08% EDTA in PBS and replated for further passage. Those from Passage 2 were stocked as primary MEFs. Spontaneously immortalized MEFs were established after single colony isolation during 30–40 passages. Their genotypes were determined by genomic polymerase chain reaction (PCR) amplification and three lines of immortalized MEFs were independently established from three embryos for each genotype.

Cell proliferation assays

Primary or immortalized MEFs were seeded at 1×10^5 cells (Figures 1C and 4A) or 0.5×10^5 cells (Figure 7C) per well in six-well plates (Nalge Nunc International K.K., Tokyo, Japan). Cells were harvested every 2 days or every day, respectively, and the numbers of cells were counted using a hemocytometer.

Cell-cycle analysis

Flow cytometric analysis of the cell cycle was performed as described (13). Cells (1×10^6 cells per assay) were centrifuged, washed with phosphate buffered saline (PBS) and suspended in PBS containing 0.2% Triton X-100. We then added 5 μl of RNase A (1 mg/ml) and 50 μl of propidium iodide (PI, 1 mg/ml). DNA content and cell numbers were analyzed with an LSR flow cytometer (Becton Dickinson, San Jose, CA, USA). The

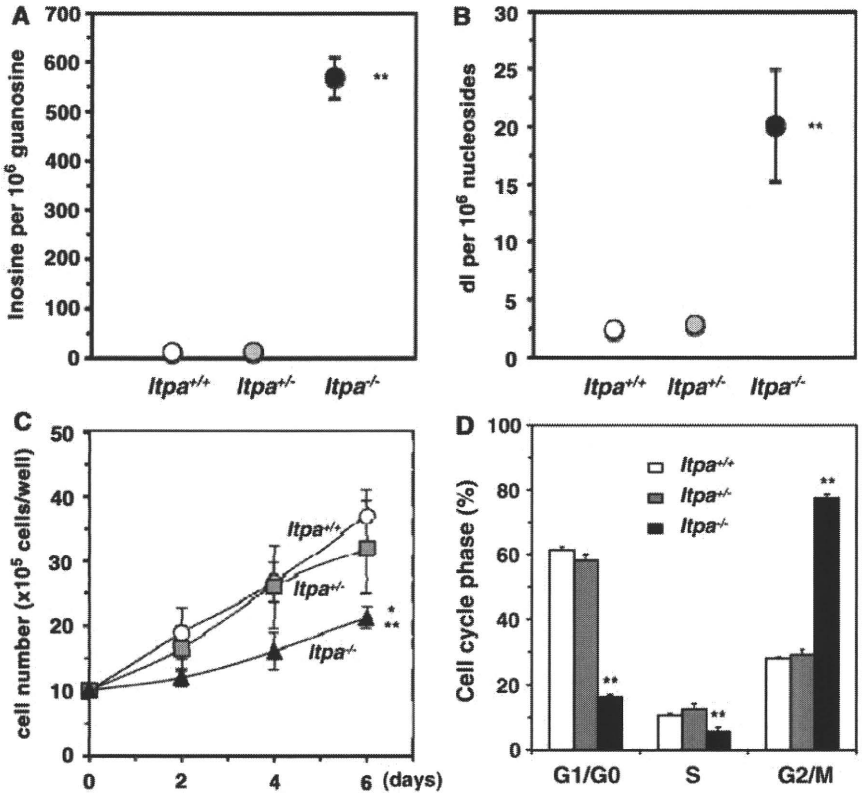

Figure 1. ITPA-deficient primary MEFs exhibit various cellular dysfunctions. (**A**) ITPA deficiency caused a significantly increased accumulation of inosine in cellular RNA. Inosine level was determined by LC–MS/MS analysis of cellular RNA prepared from embryos (N3). Result of non-repeated measures ANOVA (two-tailed), $P = 1.69 \times 10^{-7}$. Student–Newman–Keuls (SNK) *post hoc* test, $^{**}P < 0.01$ (versus $Itpa^{+/+}$ and $Itpa^{+/-}$). Data are shown as the mean ± SD ($n = 3$ independent embryos). (**B**) ITPA deficiency caused a significantly increased accumulation of deoxyinosine (dI) in nuclear DNA. Deoxyinosine (dI) level was determined by LC–MS/MS analysis of nuclear DNA prepared from embryos (N3). Result of non-repeated measures ANOVA (two-tailed), $P = 0.00038$. SNK *post hoc* test, $^{**}P < 0.01$ (versus $Itpa^{+/+}$ and $Itpa^{+/-}$). Data are shown as the mean ± SD ($n = 3$ independent embryos). (**C**) ITPA deficiency impairs normal cell proliferation. Primary MEFs (Passage 2) isolated from four separate $Itpa^{-/-}$ embryos showed significant prolonged doubling time in comparison to those from $Itpa^{+/+}$ and $Itpa^{+/-}$ embryos. Result of repeated measures ANOVA (two-tailed), $P = 0.0005$. Bonferroni/Dunn *post-hoc* test, $^{*}P < 0.05$ (versus $Itpa^{+/-}$), $^{**}P < 0.01$ (versus $Itpa^{+/+}$). Data are shown as the mean ± SD ($n = 4$ independent MEFs). (**D**) ITPA deficiency causes G2/M arrest. Primary MEFs (Passage 5) were subjected to flow cytometry analysis and the percentages of Cell-cycle phases in each MEF set were determined. Result of non-repeated measures ANOVA (two-tailed), $P = 1.74 \times 10^{-8}$. Bonferroni *post hoc* test, $^{**}P < 0.01$ (versus $Itpa^{+/+}$ and $Itpa^{+/-}$). Data are shown as the mean ± SD ($n = 3$ independent isolates).

data were analyzed using CellQuest and ModFit software (Becton Dickinson).

Karyotype analysis

A 50% confluent culture of MEFs was treated with 0.1 μg/ml colcemid (Nacalai Tesque Inc., Kyoto, Japan) for 30 min. After hypotonic treatment of harvested cells in 75 mM KCl, cells were fixed in freshly prepared Carnoy's fixative (methanol:acetic acid 3:1), and the cell suspension was dropped onto a glass slide, air-dried and immediately stained with freshly prepared Giemsa staining solution (Merck KGaA, Darmstadt, Germany cat. no. 1.09204.0509, 25× diluted in PBS) for 20 min. After rinsing the slide in PBS twice and in distilled water twice, air-dried slides were cover-slipped using Permount (Fisher Scientific, Waltham, MA, USA; SP15-100). The slide was observed under an Axioscope 2 plus microscope equipped with AxioCam and AxioVision software (Carl Zeiss MicroImaging Japan, Tokyo, Japan). A total 30 cells in metaphase was examined for each preparation.

Quantification of deoxyinosine or inosine by liquid chromatography coupled with tandem mass spectrometry

The preparation and digestion of nuclear DNA samples were as described (14), except that 10 mM 2, 2, 6, 6-tetramethylpiperidine-*N*-oxyl (TEMPO, Wako Pure Chemicals) and 20 μM 2′-deoxycoformycin (a kind gift from the Chemo-Sero-Therapeutic Research Institute, Kumamoto, Japan), an adenosine deaminase inhibitor, was added at all stages of manipulation, as described by Taghizadeh *et al.* (15). RNA was prepared using RNeasy Mini Kits (Qiagen Inc., Valencia, CA, USA) according to the manufacturer's instructions in the presence of 20 mM TEMPO and 20 μM 2′-deoxycoformycin. DNA or RNA samples were digested with nuclease P1 (Yamasa, Chiba, Japan) and alkaline phosphatase (Sigma-Aldrich, P-5521) and digested samples were subjected to LC–MS/MS

analysis using the Shimadzu VP-10 HPLC system (SHIMADZU CORPORATION, Kyoto Japan) connected to the API3000 MS/MS system (PE-SCIEX, Applied Biosystems, Foster City, CA, USA), as described (14).

Immunostaining

To detect single-stranded (ss) DNA, the slides were incubated with anti-ssDNA (IBL, Takasaki, Japan; code number 18 731, 1/100 dilution) in combination with Alexa Fluor 488-conjugated goat anti-rabbit IgG (Invitrogen, Carlsbad, CA. USA), as described (16). Nuclei were counterstained with 4′, 6-diamino-2-phenylindole (DAPI, 50 ng/ml; Vector, Burlingame, CA, USA). A cover slide was mounted onto the slide with Vectashield (Vector). The slide was observed using an Axioskop 2 plus microscope equipped with AxioCam and AxioVision software (Carl Zeiss MicroImaging Japan). A total of 100 cells were examined for each preparation.

Inosine triphosphatase and Inosine diphosphatase assays

Embryo samples or pellets of immortalized MEFs (1×10^7 cells) were washed twice with PBS and quickly frozen in liquid nitrogen. Frozen samples in 100 µl of lysis buffer containing 50 mM Tris–HCl (pH 8.0), 50 mM NaCl, 1 mM dithiothreitol and protease inhibitor cocktail (Nacalai Tesque), were sonicated at 4°C. The lysate was centrifuged at 17 360 × *g* for 60 min and the supernatant was collected as a crude cell extract. The protein concentration was determined with a Protein Assay system (Bio-Rad, Hercules, CA, USA) using bovine serum albumin (Thermo Fisher Scientific Inc., Waltham, MA, USA) as a standard. Inosine triphosphatase or Inosine diphosphatase activities were assayed by measuring the hydrolysis of ITP or IDP to IMP. The reaction mixture contained 50 mM Tris–HCl (pH 8.5), 50 mM $MgCl_2$, 1 mM DTT, 0.2 mM ITP or IDP and 1–10 µg of the crude-cell extract to be examined. The reaction was run at 30°C for 20 min and stopped by adding 150 mM EDTA. The reaction mixture was applied to HPLC analysis as described (6). Separation and quantification of nucleotides were performed by HPLC using a Waters Alliance 2690 separation module equipped with a Model 996 photodiode array detector. A buffer consisting of 75 mM sodium phosphate (pH 6.4), 0.4 mM EDTA, with 20% acetonitrile was used as the mobile phase in a TSK-GEL DEAE-2SW column, 4.6 × 250 mm (Tosoh Corp., Tokyo, Japan).

Quantitative real-time reverse transcription polymerase chain reaction

MEFs were seeded at 1×10^5 cells per well with 500 µl of medium in 24-well plates and cultured to 70–80% confluency, or for 3 days. RNA was extracted from the harvested cells using an Isogen kit (Nippon Gene Inc., Tokyo, Japan). Totally 2 µg of total RNA was subjected to RNase-free DNase I treatment and cDNA synthesis using random decamers and a Cells-to-cDNA II kit (Ambion), according to the manufacturer's instructions. Quantitative real-time PCR was performed using an ABI Prism 7000 sequence detection system with 10 ng cDNA, a set of *Nudt16* primers (FmNud3RT, RmNud3RT; 200 nM) or a set of *Gapdh* primers (F-Gapdh, R-Gapdh; 50 nM) and Power SYBR Green PCR Master Mix (Applied Biosystems) in a total volume of 25 µl. The PCR reaction was performed as follows: a single cycle of 50°C for 2 min, a single cycle of 95°C for 10 min, followed by 40 cycles of 95°C for 15 s and 60°C for 1 min. The primers were designed using PRIMER EXPRESS software (Applied Biosystems) and their sequences are shown in Supplementary Table S2. Specificity of the PCR products was established by dissociating curve analysis and by running the products on a 2% agarose gel to verify their size. The *Nudt16* mRNA level is expressed relative to the *Gapdh* mRNA level. Serially diluted cDNA was used to obtain a standard curve for each transcript.

Western blotting

MEFs were seeded at 5×10^5 cells per dish in 10 ml medium in a 90 mm Petri dish (Nalge Nunc International K.K.) and were cultured to 70–80% confluency or for 3 days. Cells were washed twice with PBS and harvested using 2× SDS sample buffer [125 mM Tris–HCl (pH 6.8), 4% SDS, 10% glycerol, 4% 2-mercaptoethanol]. The protein concentration was determined using a Protein Assay system as above. Protein samples were separated by SDS–PAGE and transferred to 0.45 µm Immobilon-P membrane (Millipore Inc., Madison, WI, USA) and western blot analysis using anti-hNUDT16 (1 µg/ml) or anti-ITPA antiserum (1/500 dilution) (5) with horseradish peroxidase-conjugated protein A and an ECL-Plus kit (GE Healthcare Bio-Sciences, Piscataway, NJ, USA) was performed as described (17). The same membrane was treated with WB stripping solution (Nacalai Tesque) and reprobed with anti-GAPDH (Millipore, Inc., Billerica, MA, USA; MAB374, 10^5× diluted) and HRP-anti-mouse IgG (BD Biosciences, San Jose, CA, USA).

Expression of recombinant mouse NUDT16 protein

An expression vector for the mouse NUDT16 protein was constructed by inserting the NdeI-HindIII fragment of pET28a(+):mNudt16 into the NdeI-HindIII region of pET32a(+) (Merck KGaA), thus Trx·Tag-His·Tag-S·Tag sequences were removed. *Escherichia coli* BL21 cells were transfected with pET32a(+) vector or pET32a:mNudt16 using a Cell-porator (Life Technologies, Carlsbad, CA, USA) according to the manufacturer's instructions. Transformants were selected on LB-agar plates in the presence of 30 µg/ml ampicillin. Established transformants were cultured until the OD_{600} reached 0.6 and then incubated with 1 mM isopropyl β-D-thiogalactoside for a further 3 h. Cells were harvested by centrifugation and resuspended in 1 ml of 2× SDS sample buffer. Samples were subjected to 12.5% SDS–PAGE and the expression of mouse NUDT16 protein without tag was confirmed by western blotting.

Introduction of silencing RNA into immortalized MEFs

Nudt16 siRNA (Ambion/Applied Biosystems, Austin, TX, USA; *Silencer* Select; s93780, s93782, 25 μM) or control siRNA (Ambion/Applied Biosystems, *Silencer* Select Negative Control #1 siRNA, cat. no. 4390844) was introduced into immortalized MEFs ($Itpa^{+/+}$, $Itpa^{-/-}$) by electroporation using a MicroPorator-mini (Digital Bio Technology, Seoul, Korea, MP-100, 1100 V, 10 ms for 2 pulses) and cells were replated appropriately into six-well plates 1 day after electroporation for further analysis.

Statistical analysis

Statistical analysis was performed using Stat View 5.0 (SAS Institute Inc., Cary, NC, USA). The statistical significance between two groups was determined with Student's *t*-test, and that among more than three groups was determined with non-repeated or repeated measures ANOVA with an appropriate correction for multiple comparisons as described in each figure legend. *P*-values <0.05 are considered statistically significant.

RESULTS

ITPA deficient primary MEFs exhibit various cellular dysfunctions

$Itpa^{-/-}$ mice with a 129·C57BL/6J mixed genetic background exhibited incomplete embryonic lethality and the surviving pups die about 2 weeks after birth with growth retardation and heart failure (6). After backcrossing the heterozygotes ($Itpa^{+/-}$) to C57BL/6J mice for more than five generations (N5), intercrosses of the obtained $Itpa^{+/-}$ mice yielded $Itpa^{-/-}$ embryos in uterus in accordance with Mendel's laws until embryonic gestation day (E) 18, but there were few newborn pups (Supplementary Table S1), indicating that ITPA deficiency causes perinatal lethality in a C57BL/6J genetic background.

We confirmed significantly increased accumulation of inosine (567.3 ± 41.4 residues per 10^6 guanosine) in cellular RNA prepared from $Itpa^{-/-}$ embryos (N14) in comparison to those from $Itpa^{+/+}$ (10.5 ± 1.50) and $Itpa^{+/-}$ (11.4 ± 1.07) embryos by liquid chromatography coupled with tandem mass spectrometry (LC–MS/MS) analysis (Figure 1A), as previously observed in various tissues of surviving $Itpa^{-/-}$ pups (6).

Furthermore, LC–MS/MS analysis of nuclear DNA prepared from embryos revealed that $Itpa^{-/-}$ embryos (E14.5) obtained from intercrosses of $Itpa^{+/-}$ mice (N3) contained significantly more dI in their nuclear DNA (20.1 ± 4.8 residues per 10^6 nucleosides): more than eight times that measured in $Itpa^{+/+}$ embryos (2.34 ± 0.76) (Figure 1B). The increased dI levels were also confirmed in $Itpa^{-/-}$ embryos after further backcrossing to C57BL/6J mice (N14, E13.5, 24.5 ± 2.24 dI residues per 10^6 nucleosides).

To examine the nature of the cellular dysfunction caused by ITPA deficiency, we isolated embryos (at E13.5 and E14.5) from intercrosses of $Itpa^{+/-}$ littermates (N10, one pair; N11, two pairs) and determined their genotypes (Supplementary Table S1). Among 20 embryos, five were found to be $Itpa^{-/-}$, 10 were $Itpa^{+/-}$ and the remaining five were $Itpa^{+/+}$. Then we isolated primary MEFs independently from four embryos of each genotype and their genotypes and the expression levels of ITPA protein were confirmed (Supplementary Figure S1A and B). All $Itpa^{-/-}$ primary MEFs at the second passage showed significantly longer doubling time (132.0 ± 14.6 h) than those from $Itpa^{+/+}$ (78.6 ± 10.1 h) and $Itpa^{+/-}$ (87.5 ± 14.3 h) embryos (Figure 1C). There was no obvious difference in their morphology under phase contrast microscopy (Supplementary Figure S1C). In Passage 5, we observed essentially the same proliferation deficiency in $Itpa^{-/-}$ MEFs and slightly increased numbers of senescence-associated β-galactosidase (SA-β-Gal)-positive cells in $Itpa^{-/-}$ MEFs ($Itpa^{+/+}$ versus $Itpa^{-/-}$, 3.64% versus 7.74%; Supplementary Figure S2A and B). Flow cytometry analysis of the cell cycle revealed that $Itpa^{-/-}$ MEFs exhibited a significant increase in the G2/M phase ($Itpa^{+/+}$ versus $Itpa^{-/-}$, 28.4% versus 77.4%; Figure 1D) and a slight increase in the sub G1 fraction ($Itpa^{+/+}$ versus $Itpa^{-/-}$, 1.61% versus 5.51%; fraction M1 in Figure 2A). There was an apparent increase in cells with an abnormally increased DNA content in $Itpa^{-/-}$ MEFs compared with $Itpa^{+/+}$ MEFs (fraction M3 in Figure 2A), indicating that the G2/M phase shown in Figure 1D might have contained some tetraploid cells at the G1 phase (Figure 2B). There was no increase in dead cells detected as propidium iodide (PI)/Hoechst-double positive cells (Supplementary Figure S2C). These results indicate that ITPA deficiency caused delay or arrest in cell-cycle progression. We further observed that exposure of $Itpa^{-/-}$, but not $Itpa^{+/+}$, $Itpa^{+/-}$ MEFs, to sodium nitrite ($NaNO_2$), which causes predominant deamination of purine bases (18), resulted in growth suppression without inducing cell death (Supplementary Figure S2C).

We next examined for chromosomal abnormalities in mitotic cells (Figure 3A). As shown in Figure 3B, chromosomal structural abnormalities were more frequently observed in $Itpa^{-/-}$ MEFs than in $Itpa^{+/+}$ MEFs, especially premature centromere separation (3.33 times more common), chromatid gaps (2.04 times) and chromatid breakages (1.52 times). Moreover, the percentage of cells with abnormal chromosomes in $Itpa^{-/-}$ primary MEFs was significantly higher than among $Itpa^{+/+}$ and $Itpa^{+/-}$ MEFs. There was an increase in ploidy abnormalities among $Itpa^{-/-}$ primary MEFs (Figure 2B): thus 41.2% in the mitotic fraction exhibited tetraploidy, while about 25% of mitotic fractions in $Itpa^{+/+}$ and $Itpa^{+/-}$ MEFs were detected as tetraploids. This confirmed the increase in ploidy among $Itpa^{-/-}$ MEFs.

Because chromatid gaps or breakages are most likely to be caused by the accumulation of single- or double-strand breaks in DNA, we examined levels of single-strand breaks (SSBs) in DNA using an antibody against single-stranded (ss) DNA (anti-ssDNA) (Figure 3C) (16). Immunofluorescence microscopy with anti-ssDNA revealed that the percentages of immunoreactive nuclei in $Itpa^{-/-}$ primary MEFs were significantly higher than in $Itpa^{+/+}$ MEFs (Figure 3D). Thus, more SSBs

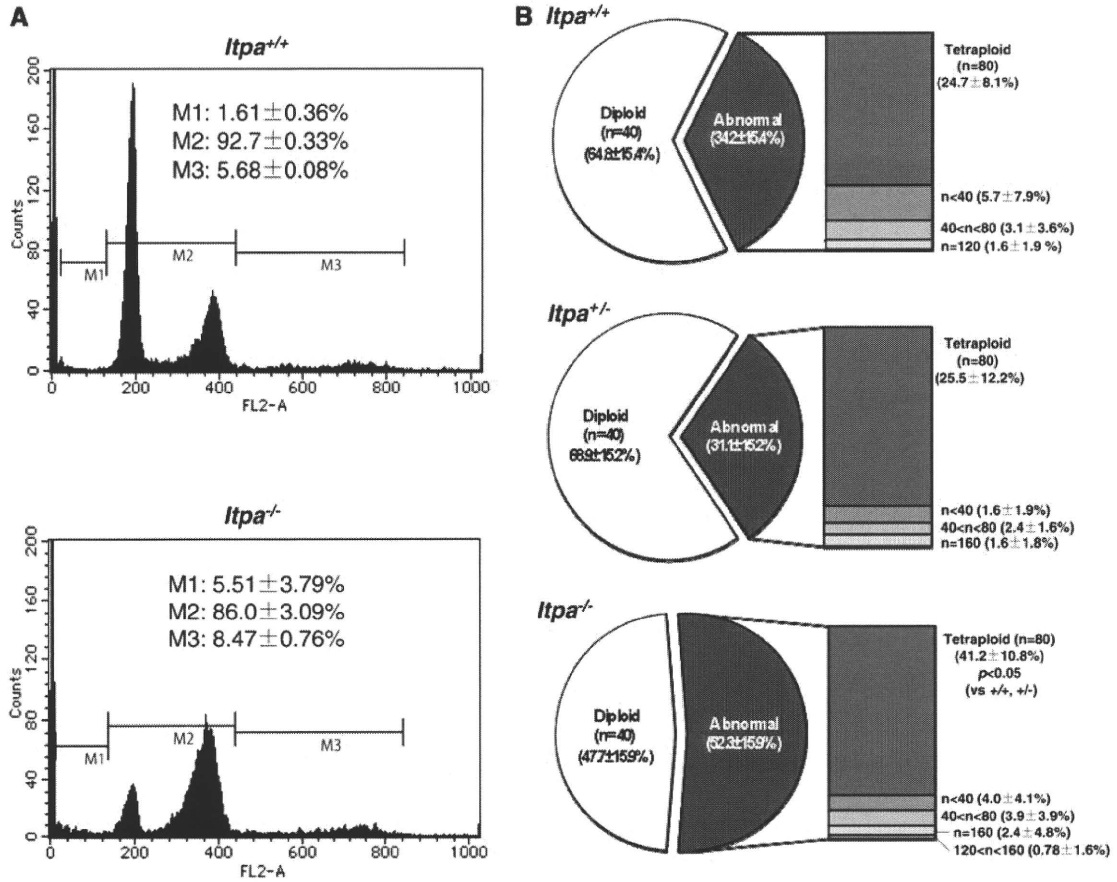

Figure 2. Increased DNA content in ITPA deficient primary MEFs. (**A**) Flow cytometric analysis of the cell cycle was performed and the sub G1 fraction (M1), diploid fraction (M2) and a fraction with an increased DNA content (M3) were determined. (**B**) ITPA deficiency increased chromosomal ploidy in primary MEFs. Percentages of diploid, tetraploid and others are shown in pie charts with the mean ± SD (three independent isolates). The frequency of tetraploidy was increased significantly in $Itpa^{-/-}$ MEFs. Results show non-repeated measures ANOVA (two-tailed): $P = 0.094$. *P*-value is shown following a Bonferroni *post hoc* test.

had accumulated in the DNA of $Itpa^{-/-}$ primary MEFs. Furthermore, the nuclei were heterogeneous in $Itpa^{-/-}$ MEFs and both the small and large nuclei exhibited ssDNA immunoreactivity (Figure 3C).

Immortalization of $Itpa^{-/-}$ MEFs reversed the ITPA-deficient phenotypes with increased ITP/IDP-hydrolyzing activity

To obtain established cell lines with ITPA deficiency, spontaneously-immortalized MEFs were isolated after 30–40 passages of each primary MEF line. We noticed that each immortalized MEF population showed the same proliferation rate, irrespective of their genotype (Figure 4A). The extent of chromosomal abnormalities (Figure 4B), and both levels of dI (2.49 ± 0.24 dI residues per 10^6 nucleosides) and ssDNA (positive in $6.17 \pm 0.68\%$ of cells) in nuclear DNA (Figure 7E and F) were similarly decreased in immortalized $Itpa^{-/-}$ MEFs. Furthermore, the G1 phase fraction increased significantly in immortalized $Itpa^{-/-}$ MEFs (Figure 5A) compared with primary MEFs (Figure 2A). Because the percentages of tetraploids were significantly higher in both primary and immortalized $Itpa^{-/-}$ MEFs than $Itpa^{+/+}$ or $Itpa^{+/-}$ MEFs (Figures 2B and 5B), the G2/M fraction in immortalized $Itpa^{-/-}$ MEFs was apparently less than in primary $Itpa^{-/-}$ MEFs.

To test whether any backup enzyme for ITPA deficiency might exist in the immortalized $Itpa^{-/-}$ MEFs, we measured ITP-hydrolyzing activity in extracts prepared from embryos and immortalized MEFs (Table 1, Supplementary Figure S3). There was no detectable ITP-hydrolyzing activity in extracts prepared from $Itpa^{-/-}$ embryos, but a significantly high rate was detected in $Itpa^{+/+}$ embryos, thus confirming ITPA deficiency in $Itpa^{-/-}$ embryos. We also confirmed that $Itpa^{-/-}$ primary MEFs (Passage 3) did not generate IMP from ITP. On the other hand, we detected substantial activity in extracts from immortalized $Itpa^{-/-}$ MEFs, although the levels were less than 20% of that detected in immortalized $Itpa^{+/+}$ MEFs or embryos. We then measured IDP-hydrolyzing activity in these extracts (Table 1, Supplementary Figure S3). Levels were increased both in $Itpa^{+/+}$ and $Itpa^{-/-}$ MEFs during immortalization and the activity was more significantly increased in immortalized $Itpa^{-/-}$ MEFs than in immortalized $Itpa^{+/+}$ MEFs. These results strongly suggest that an increased

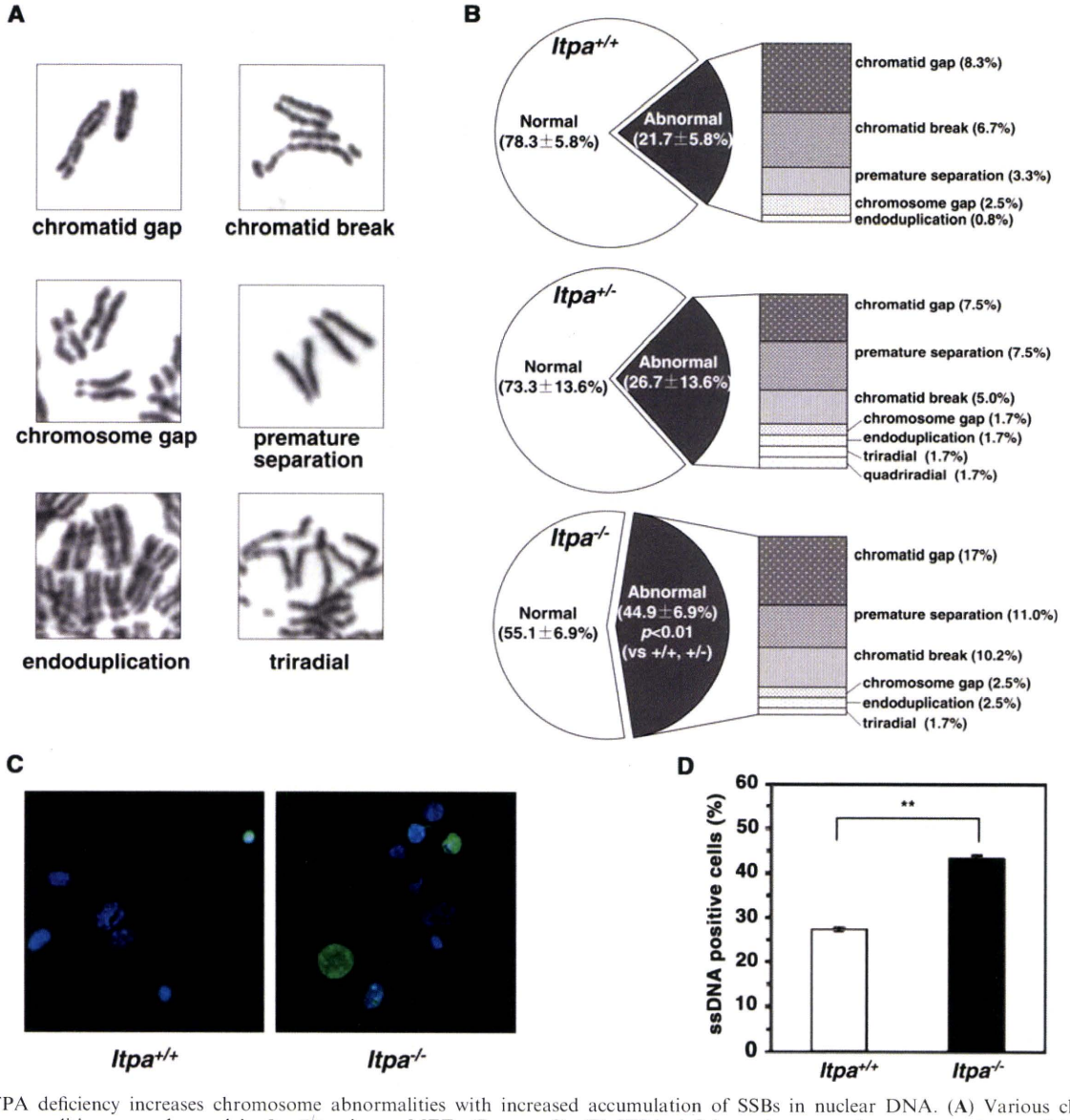

Figure 3. ITPA deficiency increases chromosome abnormalities with increased accumulation of SSBs in nuclear DNA. (**A**) Various chromosome structural abnormalities were observed in $Itpa^{-/-}$ primary MEFs (Passage 2). (**B**) ITPA deficiency increases chromosome abnormalities. The frequency of chromosomal abnormality was significantly increased in $Itpa^{-/-}$ MEFs in comparison to $Itpa^{+/+}$ and $Itpa^{+/-}$ MEFs. Result of non-repeated measures ANOVA (two-tailed), $P = 0.0149$. Bonferroni *post hoc* test, $P < 0.01$. Data are shown as pie charts with the mean ± SD ($n = 4$ independent isolates). (**C**) Detection of immunoreactivity against ssDNA in $Itpa^{-/-}$ primary MEFs. Immunofluorescence microscopy with anti-ssDNA antibody (green) revealed significantly increased ssDNA immunoreactivity in nuclei (DAPI, blue) of $Itpa^{-/-}$ primary MEFs (Passage 2) compared with the wild-type ($Itpa^{+/+}$). (**D**) Significant Increase in the ssDNA-positive population in $Itpa^{-/-}$ primary MEF tested by unpaired Student's *t*-test (two-tailed): $^{**}P < 0.01$. Data are shown in a bar graph (mean ± SD, $n = 4$ independent isolates).

expression of IDP or ITP-hydrolyzing enzyme(s) blocked or reversed the ITPA-deficient phenotypes observed in primary $Itpa^{-/-}$ MEFs.

NUDT16 with strong (deoxy)inosine diphosphatase activity is responsible for cancellation of ITPA-deficient phenotypes and an increase in ITP/IDP-hydrolyzing activity during immortalization

We recently found that the human NUDT16 (nudix [nucleoside diphosphate linked moiety X]-type motif 16) protein, identified as an ITP/XTP/GTP binding protein, has strong IDP and 2′-deoxy-IDP (dIDP)-hydrolyzing activities with weak ITP/dITP-hydrolyzing activities. We also confirmed that mouse NUDT16 protein has essentially the same activities as the human protein (Iyama *et al.*, in preparation). Therefore, we compared *Nudt16* mRNA levels among primary and immortalized $Itpa^{+/+}$ or $Itpa^{-/-}$ MEFs (Figure 6A). Quantitative real-time reverse transcription polymerase chain reaction (RT–PCR) analysis revealed that the expression levels of *Nudt16* mRNA were similar between primary MEFs derived from $Itpa^{+/+}$ and $Itpa^{-/-}$ embryos. In contrast, the expression levels of *Nudt16* mRNA in immortalized $Itpa^{-/-}$ MEFs were more than 3-fold higher than those of primary $Itpa^{-/-}$ MEFs and more than 2-fold higher

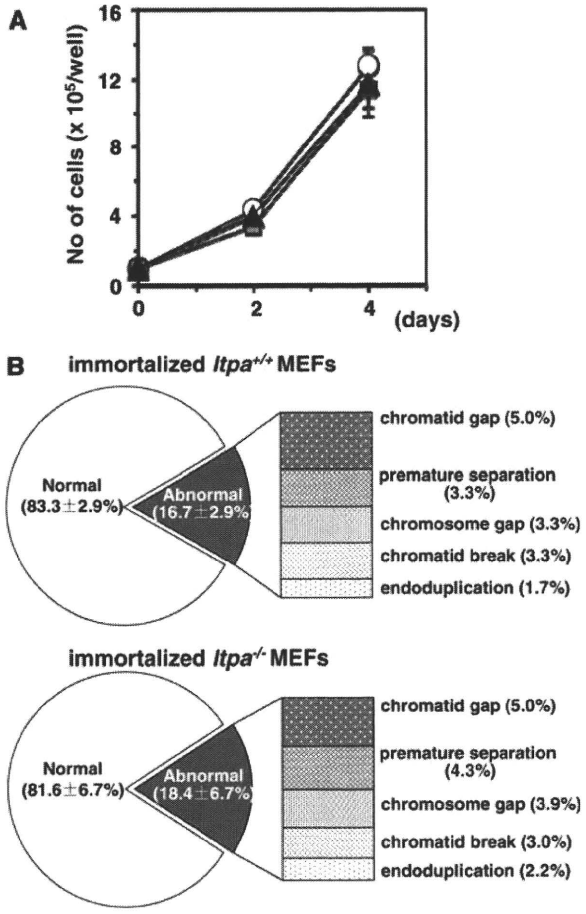

Figure 4. ITPA-deficient phenotypes are reversed during immortalization. (**A**) Immortalized $Itpa^{-/-}$ MEFs (triangle) showed the same proliferation rate as did immortalized $Itpa^{+/+}$ (circle) and $Itpa^{+/-}$ (square) MEFs. Error bars represent the SD ($n = 3$ independent isolates). (**B**) The frequency of chromosomal abnormalities was decreased in immortalized $Itpa^{-/-}$ MEFs to the levels seen in immortalized $Itpa^{+/+}$ MEFs. Data are shown as the mean ± SD ($n = 3$ independent isolates).

than those in immortalized $Itpa^{+/+}$ MEFs (Figure 6A). Significantly increased expression of NUDT16 protein in immortalized $Itpa^{-/-}$ MEFs was confirmed by western blotting analysis of crude cell extracts prepared from these MEFs (Figure 6B). We thus conclude that the increased expression of *Nudt16* in immortalized $Itpa^{-/-}$ MEFs is responsible for the increase in ITP/IDP-hydrolyzing activity compared with immortalized $Itpa^{+/+}$ MEFs.

To examine the contribution of NUDT16 to the reversal of ITPA-deficient phenotypes in immortalized $Itpa^{-/-}$ MEFs, knockdown of *Nudt16* mRNA expression was performed using a mixture of two different *Nudt16* silencing (si)RNAs. This treatment caused an efficient reduction of both *Nudt16* mRNA and protein levels to less than 20% of the levels seen in controls (Figure 7A and B). Knockdown of *Nudt16* expression in immortalized $Itpa^{-/-}$ but not in $Itpa^{+/+}$ MEFs caused a significant reduction in proliferation rate (Figure 7C), as observed in primary $Itpa^{-/-}$ MEFs (Figure 1C).

We next measured inosine levels in cellular RNA with or without *Nudt16* siRNAs. Immortalized $Itpa^{-/-}$ MEFs contained 516.8 ± 22.3 inosine residues per 10^6 guanosine residues of RNA in the presence of control siRNA which was slightly lower than that in $Itpa^{-/-}$ embryos (567.3 ± 41.4 residues per 10^6 guanosine), and *Nudt16* expression knockdown increased the level to 648.5 ± 01.7 residues per 10^6 guanosine residues of RNA (Figure 7D). As shown in Figure 7E, immortalized $Itpa^{-/-}$ MEFs contained 2.49 ± 0.24 dI residues per 10^6 nucleosides in nuclear DNA in the presence of control siRNA which was equivalent to that in immortalized $Itpa^{+/+}$ MEFs (2.74 ± 0.17 dI residues per 10^6 nucleosides). *Nudt16* expression knockdown in immortalized $Itpa^{-/-}$ MEFs significantly increased the level more than 5-fold (12.73 ± 0.99 residues per 10^6 nucleosides). In contrast, knockdown of *Nudt16* expression in immortalized $Itpa^{+/+}$ MEFs did not affect the level of dI accumulation in nuclear DNA (2.96 ± 0.3 dI residues per 10^6 nucleosides).

Knockdown of *Nudt16* expression significantly increased the immunoreactivity against ssDNA in immortalized $Itpa^{-/-}$ MEFs (Figure 7F). Moreover, karyotyping of immortalized $Itpa^{-/-}$ MEFs after *Nudt16* expression knockdown revealed a significant increase in chromosome structural abnormalities, such as chromatid gaps, premature separation and triradial forms compared with controls (Figure 7G).

Thus, increased expression of *Nudt16* was responsible for reversal of the ITPA-deficient phenotypes with reduction of dI accumulation in nuclear DNA but not inosine in cellular RNA.

DISCUSSION

ITPA deficiency increases the accumulation of deoxyinosine in nuclear DNA resulting in severe cellular dysfunction

Here, we showed for the first time that ITPA deficiency caused a significant accumulation of dI in the nuclear DNA of mouse embryos, most of which are likely to die around the time of birth. In wild-type embryos, fewer than three residues of dI per 10^6 nucleosides, corresponding to about 20 000 residues in a whole cell, were detected in nuclear DNA, whereas about 20 residues of dI per 10^6 nucleosides reaching more than 10^5 residues per cell accumulated in $Itpa^{-/-}$ embryos. These results indicate that both spontaneous generation of dITP and incorporation of dITP into DNA occurred at significantly high frequencies. Thus, ITPA deficiency caused severe cellular dysfunction resulting in perinatal lethality. Indeed, we demonstrated that this deficiency in primary MEFs increased the accumulation of SSBs in nuclear DNA detected as ssDNA immunoreactivity and as chromosomal abnormalities such as chromatid/chromosome gaps or breaks. There was also premature centromere separation. All these chromosomal anomalies are likely to cause G2/M arrest thus suppressing cell proliferation, as observed in primary $Itpa^{-/-}$ MEFs.

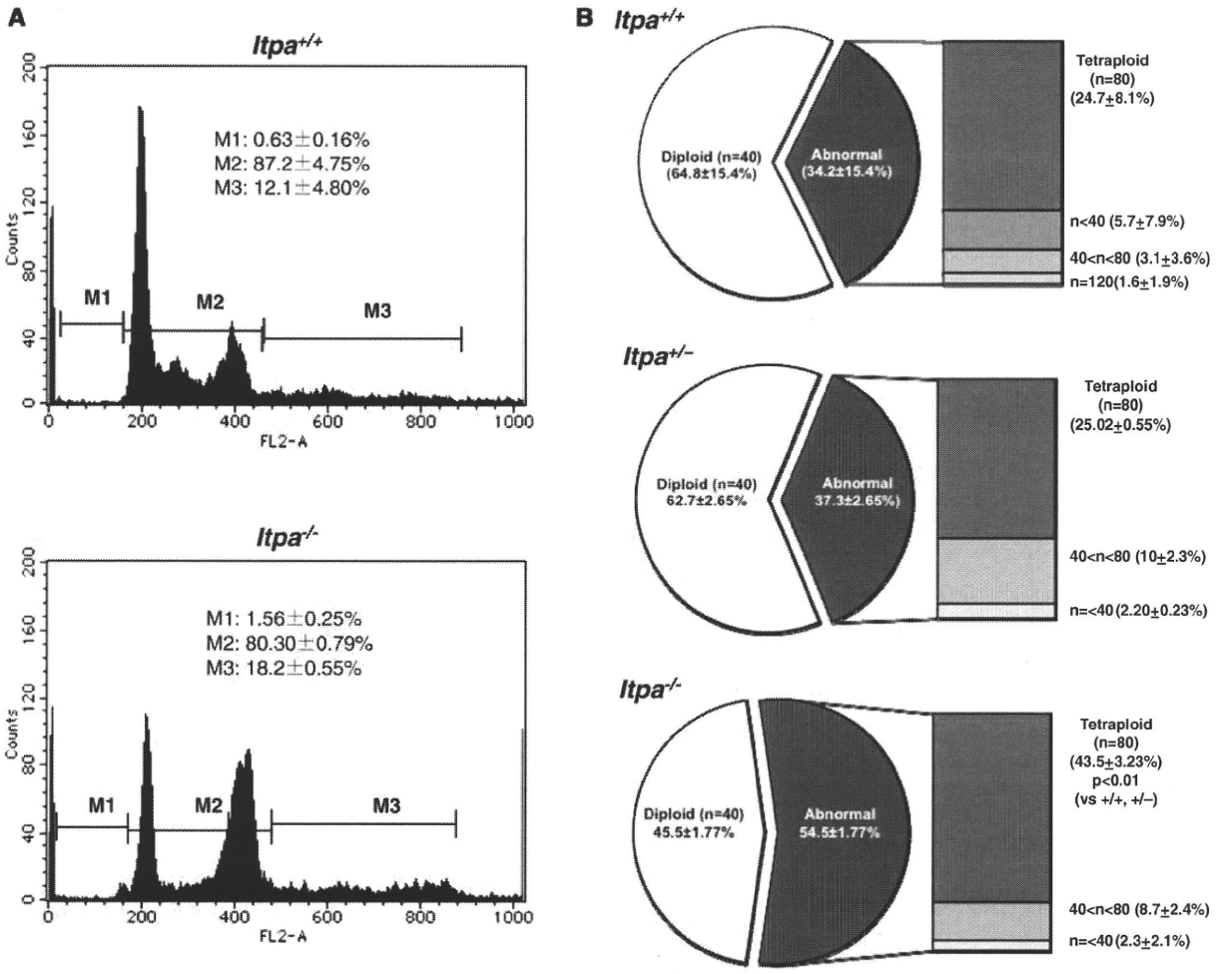

Figure 5. Increased DNA content in ITPA deficient immortalized MEFs. (**A**) Flow cytometric analysis of the cell cycle was performed and the sub G1 fraction (M1), diploid fraction (M2) and a fraction with an increased DNA content (M3) were determined. (**B**) ITPA deficiency increased chromosomal ploidy in immortalized MEFs. Percentages of diploid, tetraploid and others are shown in pie charts with the mean ± SD (three independent isolates). The frequency of tetraploidy was increased significantly in *Itpa*$^{-/-}$ MEFs. Results show non-repeated measures ANOVA (two-tailed): $P = 0.00015$. *P*-values are shown following a Bonferroni *post hoc* test.

Table 1. Specific ITP/IDP hydrolysis activity in crude-cell extracts prepared from embryos and immortalized MEFs

Cell extract	Substrate	Isolate no. 1		Isolate no. 2	
		Specific activity (u/μg)	SD	Specific activity (u/μg)	SD
Itpa$^{+/+}$ embryo	ITP	6.34	0.8	4.08	0.7
Itpa$^{+/+}$ embryo	IDP	0.84	0.2	1.26	0.4
Itpa$^{+/+}$ iMEF	ITP	6.42	0.9	7.24	1.0
Itpa$^{+/+}$ iMEF	IDP	3.49	0.5	3.68	0.4
Itpa$^{-/-}$ embryo	ITP	ND		ND	
Itpa$^{-/-}$ embryo	IDP	0.86	0.3	1.85	0.4
Itpa$^{-/-}$ iMEF	ITP	1.09	0.1	1.36	0.3
Itpa$^{-/-}$ iMEF	IDP	5.90	0.5	7.85	1.5

As a measure,1 unit (u) was defined as the level of activity producing 1 pmol of IMP at 30°C for 1 min with 0.2 mM ITP/IDP, pH = 8.0, $n = 3$. Key: ND, not detected; iMEFs, immortalized MEFs.

In *E. coli*, the lethality of *rdgB recA* or *rdgB recBC* double mutants, the former-encoding inosine triphosphatase, is suppressed by the inactivation of endonuclease V (EndoV) (12), which cleaves at the second phosphodiester bond at 3′ to dI and initiates nucleotide excision repair (19). It is likely that an inosine triphosphatase deficiency in *E. coli* results in the accumulation of its substrate nucleotides, dITP in the nucleotide pools, thus causing an increased accumulation of dI into DNA. Further excision repair initiated by EndoV leads to chromosomal fragmentation in *recA* or *recBC* mutants.

In mammals, there are at least two enzymes that might be involved in excision repair of dI: the mammalian homolog of EndoV and alkyladenine DNA glycosylase (AAG) which can excise hypoxanthine, a deaminated adenine base (20–24). Because mammalian cells are likely to be less efficient in recombination repair than *E. coli* (25), ITPA deficiency itself thus causes severe

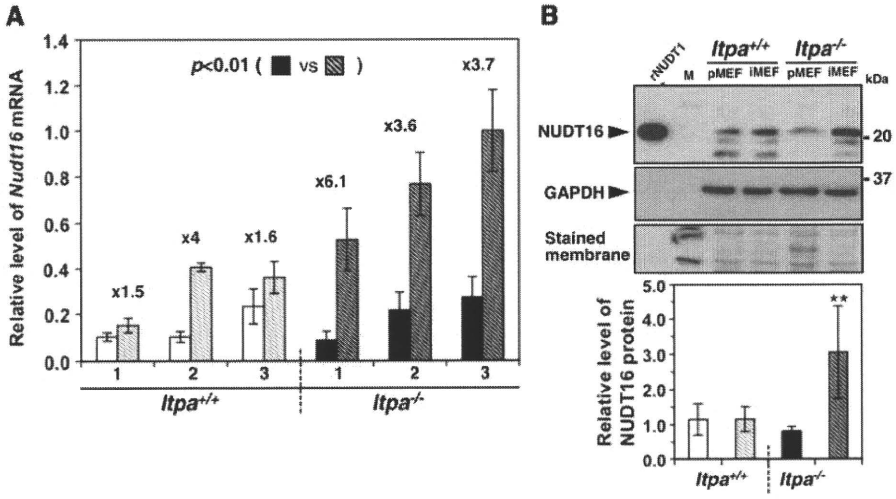

Figure 6. NUDT16 with strong dIDP/IDP-hydrolyzing activity is the back-up enzyme responsible for the cancellation of ITPA-deficient phenotypes during immortalization. (**A**) Expression of *Nudt16* mRNA. Quantitative real-time RT–PCR was performed to compare *Nudt16* mRNA levels between primary (passage 3) and immortalized MEFs. Levels of *Nudt16* mRNA were normalized to those of *Gapdh* mRNA. Values relative to the highest level of *Nudt16* mRNA in immortalized $Itpa^{-/-}$ MEFs (isolate No. 3) are shown. Unpaired Student's *t*-test (two-tailed) showed $P < 0.01$ between primary and immortalized $Itpa^{-/-}$ MEFs. Data are shown in a bar graph (mean ± SD), with fold changes between primary and immortalized MEFs ($n = 3$ independent isolates). Open and black bars show primary MEFs; shaded bars indicate immortalized MEFs. (**B**) Expression of NUDT16 protein. Western blotting was performed for crude cell extracts (40 μg) prepared from primary (Passage 2) and immortalized MEFs, using anti-NUDT16 antibody (top). GAPDH was detected as an internal control (middle). Membranes were stained with Gel Code Blue in order to confirm the loading and transfer (bottom). Intensities of NUDT16 bands were measured and relative levels normalized to GAPDH are shown in a bar graph. Open and black bars show primary MEFs; shaded bars indicate immortalized MEFs. Result of non-repeated measures ANOVA (two-tailed), $P < 0.019$. Bonferroni *post hoc* test, $^{**}P < 0.01$ (versus others). Error bars represent the SD ($n = 3$ independent isolates).

phenotypes with massive generation of SSBs in DNA, likely caused by efficient excision repair of dI or hypoxanthine.

In primary $Itpa^{-/-}$ MEFs, increased frequency of chromosomal abnormalities such as chromatid/chromosome gaps or breaks might result from increased SSB accumulation in nuclear DNA, which is likely to be caused by excision repair of accumulated dI in nuclear DNA. It is noteworthy that exposure of peripheral lymphocytes to ITP or IDP in culture were reported to cause chromosome aberrations such as chromatid breaks and gaps (26) and sister chromatid exchange (27). Although the precise mechanism inducing chromosome aberration by ITP or IDP is not known, exposure to a high concentration of ITP or IDP might also result in an increase of dI in nuclear DNA, thus increasing SSBs and chromosome abnormalities as observed in $Itpa^{-/-}$ primary MEFs. Moreover, both ITPA deficiency and exposure to ITP or IDP increase premature centromere separation (26). Increased inosine levels in cellular RNA prepared from $Itpa^{-/-}$ embryos indicated that the ITP level was also significantly increased in the absence of ITPA. Therefore, these chromosomal abnormalities might be caused by the increased level of ITP in nucleotide pool. Because sister chromatid cohesion is established by a cohesin complex composed of Rad21, Smc1α, Smc3 and two Scc3 orthologs, SA1 and SA2 (28,29) and whose reaction requires ATP, ITP might compete with ATP to disrupt sister chromatid cohesion, thus resulting in premature centromere separation and inappropriate chromatid separation.

Increased expression of *Nudt16* suppresses the ITPA-deficient phenotype during immortalization

During immortalization of $Itpa^{-/-}$ MEFs, most of the ITPA-deficient phenotype characteristics, such as prolonged doubling time, G2/M arrest, SSBs accumulation, chromosome abnormalities were canceled efficiently. This was accompanied by a significant reduction of dI accumulation in nuclear DNA. The inosine level in cellular RNA was still high in immortalized $Itpa^{-/-}$ MEFs (516.8 ± 22.3 inosine residues per 10^6 guanosine residues) as much as seen in $Itpa^{-/-}$ embryos (567.3 ± 41.4 inosine residues per 10^6 guanosines), thereby indicating that the ITPA-deficient phenotypes are most likely to be attributed to the increased accumulation of dI in nuclear DNA.

We identified the human NUDT16 protein (Iyama *et al.*, manuscript in preparation) as a dIDP/IDP-hydrolyzing enzyme, which can bind ITP/XTP/GTP and efficiently hydrolyzes dIDP/IDP, and to a lesser extent dITP/ITP, to dIMP/IMP. In the present study, we found that the levels of mouse *Nudt16* mRNA and NUDT16 protein were significantly higher in immortalized $Itpa^{-/-}$ MEFs than in immortalized wild-type MEFs or primary $Itpa^{-/-}$ MEFs. Because knockdown of *Nudt16* expression efficiently reproduced the ITPA-deficient phenotypes accompanied by significant increases of dI in nuclear DNA, and to a lesser extent of inosine in cellular RNA, we conclude that NUDT16 and ITPA play a dual protective role for eliminating dITP/ITP and dIDP/IDP from nucleotide pools in mammals.

ITP can be hydrolyzed slowly to IDP by ATPase or other nucleoside triphosphatases (11,30), so increased

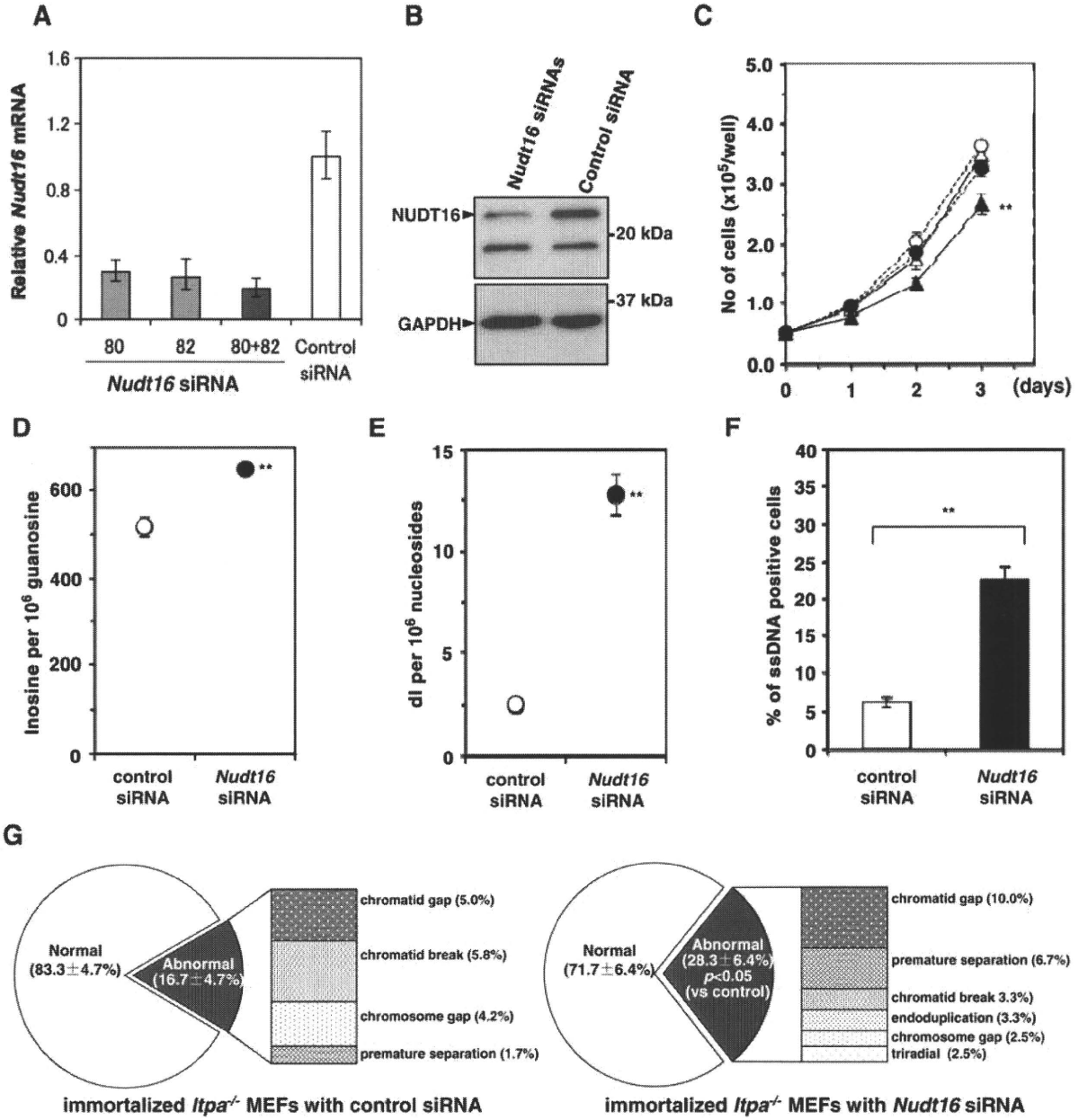

Figure 7. Knockdown of *Nudt16* mRNA suppressed ITPA-deficient phenotypes in immortalized $Itpa^{-/-}$ MEFs. (**A**) Expression of *Nudt16* mRNA. To knock down the expression of *Nudt16*, two different siRNAs (80, 82 or 80 + 82) against *Nudt16* mRNA or control siRNA were introduced into immortalized $Itpa^{-/-}$ MEFs. Forty-eight hours after the introduction, total RNA was prepared and quantitative real-time RT–PCR was performed. Levels of *Nudt16* mRNA were normalized to those of *Gapdh* mRNA and their relative values are shown. Data are shown in a bar graph (mean ± SD, $n = 3$). (**B**) Expression of NUDT16 protein. Western blotting was performed for crude cell extracts (40 μg) prepared from immortalized $Itpa^{-/-}$ MEFs treated with two *Nudt16* siRNAs (80 + 82) or control siRNA, using anti-NUDT16. GAPDH was detected as an internal control. (**C**) Knockdown of *Nudt16* mRNA suppressed proliferation of immortalized $Itpa^{-/-}$ MEFs. Expression of *Nudt16* mRNA was blocked using a mix of two different *Nudt16* siRNAs and cell proliferation was examined. Circles, $Itpa^{+/+}$; triangles, $Itpa^{-/-}$; open marks, control siRNA; closed marks, *Nudt16* siRNAs. Result of repeated measures ANOVA, two-tailed, $P < 0.0001$; Bonferroni/Dunn *post hoc* test, $^{**}P < 0.01$ (versus other three measures). Error bars represent the SD ($n = 4$). (**D**) Knockdown of *Nudt16* mRNA significantly increased the accumulation of inosine in RNA of immortalized $Itpa^{-/-}$ MEFs. Level of inosine in RNA was determined by LC–MS/MS analysis of RNA prepared from immortalized $Itpa^{-/-}$ MEFs treated with control or *Nudt16* siRNAs. Result of unpaired Student's *t*-test (two-tailed), $^{**}P < 0.01$. Data are shown as a bar graph with the mean ± SD ($n = 3$). (**E**) Knockdown of *Nudt16* mRNA significantly increased the accumulation of dI in nuclear DNA of immortalized $Itpa^{-/-}$ MEFs. Level of dI in nuclear DNA was determined by LC–MS/MS analysis of nuclear DNA prepared from immortalized $Itpa^{-/-}$ MEFs treated with control or *Nudt16* siRNAs. Result of unpaired Student's *t*-test (two-tailed), $^{**}P < 0.01$. Data are shown as a bar graph with the mean ± SD ($n = 3$). (**F**) Increased immunoreactivity against ssDNA in immortalized $Itpa^{-/-}$ MEFs after *Nudt16* knockdown. Immunofluorescence microscopy with anti-ssDNA antibody revealed significantly increased immunoreactivity after *Nudt16* knockdown. Result of unpaired Student's *t*-test (two-tailed), $^{**}P < 0.01$. Data are shown as a bar graph with the mean ± SD ($n = 4$). (**G**) Knockdown of *Nudt16* mRNA increased chromosomal abnormalities in immortalized $Itpa^{-/-}$ MEFs. The frequency of chromosomal abnormalities was increased significantly in immortalized $Itpa^{-/-}$ MEFs after *Nudt16* knockdown. Result of unpaired Student's *t*-test (two-tailed), $P < 0.05$ (versus control siRNA). Data are shown as pie charts with the mean ± SD ($n = 4$).

dIDP hydrolysis in immortalized *Itpa*$^{-/-}$ MEFs is likely to be sufficient to eliminate dITP from the nucleotide pools. Moreover, ITP can be generated in a variety of tissue extracts as well as in erythrocytes (31). We reported previously that ITP accumulated in erythrocytes but not in tissues including the heart and liver derived from *Itpa*$^{-/-}$ mice, whereas IMP accumulated markedly in RNA prepared from the latter (6). Because both RNA and DNA synthesis takes place in the latter tissues, DNA and RNA polymerases are likely to utilize ITP and dITP efficiently as nucleotide precursors, thereby consuming most of the ITP or dITP that accumulates in the nucleotide pools in the absence of ITPA.

Considering the likely source of ITP or dITP in the nucleotide pools, IMP generated from AMP by AMP deamination must be the most relevant precursor, because most cells can synthesize IDP or ITP from IMP (31) and IDP may be converted to dIDP by ribonucleotide reductase, thus generating dITP (21). To minimize accumulation of ITP or dITP in the nucleotide pools, hydrolysis of IDP or dIDP to the corresponding monophosphates catalyzed by NUDT16 is likely to be as critical as is any hydrolysis of ITP or dITP to the corresponding monophosphates.

In the present study, we showed that increased expression of NUDT16 in *Itpa*$^{-/-}$ immortalized MEFs is sufficient to cancel the ITPA-deficient phenotypes observed in *Itpa*$^{-/-}$ embryos or primary MEFs, suggesting that the lower expression level of NUDT16 in normal tissues may be why any ITPA deficiency causes such severe phenotypes. On the other hand, ITPA deficiency in humans is likely to be related to azathioprine intolerance in patients with inflammatory bowel disease, but does not cause any severe phenotype (32–34), compared with the *Itpa*$^{-/-}$ mice. It is possible that human NUDT16 expression might be higher than that in mouse, thus compensating for any ITPA deficiency.

Identification of NUDT16 as a backup enzyme for ITPA deficiency in mice will shed light on the mechanisms that enable humans to be resistant to ITPA deficiency. Towards this goal, it is important to know the relative expression of ITPA and NUDT16 in human cells and organs, and to characterize the enzymatic properties of NUDT16.

SUPPLEMENTARY DATA

Supplementary Data are available at NAR Online.

ACKNOWLEDGEMENTS

The authors thank M. Ohtsu in the Laboratory for Technical Support of our institute and N. Adachi, A. Matsuyama, K. Hayashi, K. Nakabeppu and K. Asakawa for technical assistance.

FUNDING

Ministry of Education, Culture, Sports, Science and Technology of Japan [20013034 to Y.N., 20012038 to K.S.]; the Japan Society for the Promotion of Science [19390114 to D.T., 08J03650 to T.I.]; Kyushu University Global COE program [YN]. Funding for open access charges: Ministry of Education, Culture, Sports, Science and Technology of Japan; Kyushu University Global COE program.

Conflict of interest statement. None declared.

REFERENCES

1. Nakabeppu,Y., Tsuchimoto,D., Furuichi,M. and Sakumi,K. (2004) The defense mechanisms in mammalian cells against oxidative damage in nucleic acids and their involvement in the suppression of mutagenesis and cell death. *Free Radic. Res.*, **38**, 423–429.
2. Nakabeppu,Y., Behmanesh,M., Yamaguchi,H., Yoshimura,D. and Sakumi,K. (2007) In Evans,M.D. and Cooke,M.S. (eds), *Oxidative Damage to Nucleic Acids*. Landes Bioscience/Springer, Austin, TX/New York, pp. 40–53.
3. Nakabeppu,Y. (2001) Molecular genetics and structural biology of human MutT homolog, MTH1. *Mutat. Res.*, **477**, 59–70.
4. Nakabeppu,Y., Kajitani,K., Sakamoto,K., Yamaguchi,H. and Tsuchimoto,D. (2006) MTH1, an oxidized purine nucleoside triphosphatase, prevents the cytotoxicity and neurotoxicity of oxidized purine nucleotides. *DNA Rep.*, **5**, 761–772.
5. Behmanesh,M., Sakumi,K., Tsuchimoto,D., Torisu,K., Ohnishi-Honda,Y., Rancourt,D.E. and Nakabeppu,Y. (2005) Characterization of the structure and expression of mouse *Itpa* gene and its related sequences in the mouse genome. *DNA Res.*, **12**, 39–51.
6. Behmanesh,M., Sakumi,K., Abolhassani,N., Toyokuni,S., Oka,S., Ohnishi,Y.N., Tsuchimoto,D. and Nakabeppu,Y. (2009) ITPase-deficient mice show growth retardation and die before weaning. *Cell Death Differ.*, **16**, 1315–1322.
7. Nonaka,M., Tsuchimoto,D., Sakumi,K. and Nakabeppu,Y. (2009) Mouse RS21-C6 is a mammalian 2′-deoxycytidine 5′-triphosphate pyrophosphohydrolase that prefers 5-iodocytosine. *FEBS J.*, **276**, 1654–1666.
8. Tsuzuki,T., Egashira,A., Igarashi,H., Iwakuma,T., Nakatsuru,Y., Tominaga,Y., Kawate,H., Nakao,K., Nakamura,K., Ide,F. *et al.* (2001) Spontaneous tumorigenesis in mice defective in the *MTH1* gene encoding 8-oxo-dGTPase. *Proc. Natl Acad. Sci. USA*, **98**, 11456–11461.
9. Shenoy,T.S. and Clifford,A.J. (1975) Adenine nucleotide metabolism in relation to purine enzymes in liver, erythrocytes and cultured fibroblasts. *Biochim. Biophys. Acta*, **411**, 133–143.
10. Gower,W.R. Jr, Carr,M.C. and Ives,D.H. (1979) Deoxyguanosine kinase. Distinct molecular forms in mitochondria and cytosol. *J. Biol. Chem.*, **254**, 2180–2183.
11. Burton,K., White,H. and Sleep,J. (2005) Kinetics of muscle contraction and actomyosin NTP hydrolysis from rabbit using a series of metal-nucleotide substrates. *J. Physiol.*, **563**, 689–711.
12. Bradshaw,J.S. and Kuzminov,A. (2003) RdgB acts to avoid chromosome fragmentation in *Escherichia coli*. *Mol. Microbiol.*, **48**, 1711–1725.
13. Ide,Y., Tsuchimoto,D., Tominaga,Y., Nakashima,M., Watanabe,T., Sakumi,K., Ohno,M. and Nakabeppu,Y. (2004) Growth retardation and dyslymphopoiesis accompanied by G2/M arrest in APEX2-null mice. *Blood*, **104**, 4097–4103.
14. Tsuruya,K., Furuichi,M., Tominaga,Y., Shinozaki,M., Tokumoto,M., Yoshimitsu,T., Fukuda,K., Kanai,H., Hirakata,H., Iida,M. *et al.* (2003) Accumulation of 8-oxoguanine in the cellular DNA and the alteration of the OGG1 expression during ischemia-reperfusion injury in the rat kidney. *DNA Rep.*, **2**, 211–229.
15. Taghizadeh,K., McFaline,J.L., Pang,B., Sullivan,M., Dong,M., Plummer,E. and Dedon,P.C. (2008) Quantification of DNA damage products resulting from deamination, oxidation and reaction with products of lipid peroxidation by liquid chromatography isotope dilution tandem mass spectrometry. *Nat. Protoc.*, **3**, 1287–1298.

16. Oka,S., Ohno,M., Tsuchimoto,D., Sakumi,K., Furuichi,M. and Nakabeppu,Y. (2008) Two distinct pathways of cell death triggered by oxidative damage to nuclear and mitochondrial DNAs. *EMBO J.*, **27**, 421–432.
17. Tsuchimoto,D., Sakai,Y., Sakumi,K., Nishioka,K., Sasaki,M., Fujiwara,T. and Nakabeppu,Y. (2001) Human APE2 protein is mostly localized in the nuclei and to some extent in the mitochondria, while nuclear APE2 is partly associated with proliferating cell nuclear antigen. *Nucleic Acids Res.*, **29**, 2349–2360.
18. Kow,Y.W. (2002) Repair of deaminated bases in DNA. *Free Radic. Biol. Med.*, **33**, 886–893.
19. Dalhus,B., Arvai,A.S., Rosnes,I., Olsen,Ø., Backe,P.H., Alseth,I., Gao,H., Cao,W., Tainer,J.A. and Bjørås,M. (2009) Structures of endonuclease V with DNA reveal initiation of deaminated adenine repair. *Nat. Struct. Mol. Biol.*, **16**, 138–143.
20. Karran,P. and Lindahl,T. (1978) Enzymatic excision of free hypoxanthine from polydeoxynucleotides and DNA containing deoxyinosine monophosphate residues. *J. Biol. Chem.*, **253**, 5877–5879.
21. Myrnes,B., Guddal,P.H. and Krokan,H. (1982) Metabolism of dITP in HeLa cell extracts, incorporation into DNA by isolated nuclei and release of hypoxanthine from DNA by a hypoxanthine-DNA glycosylase activity. *Nucleic Acids Res.*, **10**, 3693–3701.
22. Saparbaev,M. and Laval,J. (1994) Excision of hypoxanthine from DNA containing dIMP residues by the *Escherichia coli*, yeast, rat, and human alkylpurine DNA glycosylases. *Proc. Natl Acad. Sci. USA*, **91**, 5873–5877.
23. Moe,A., Ringvoll,J., Nordstrand,L.M., Eide,L., Bjørås,M., Seeberg,E., Rognes,T. and Klungland,A. (2003) Incision at hypoxanthine residues in DNA by a mammalian homologue of the *Escherichia coli* antimutator enzyme endonuclease V. *Nucleic Acids Res.*, **31**, 3893–3900.
24. Vallur,A.C., Maher,R.L. and Bloom,L.B. (2005) The efficiency of hypoxanthine excision by alkyladenine DNA glycosylase is altered by changes in nearest neighbor bases. *DNA Rep.*, **4**, 1088–1098.
25. Pardo,B., Gómez-González,B. and Aguilera,A. (2009) DNA double-strand break repair: how to fix a broken relationship. *Cell. Mol. Life Sci.*, **66**, 1039–1056.
26. Auclair,C., Gouyette,A., Levy,A. and Emerit,I. (1990) Clastogenic inosine nucleotide as components of the chromosome breakage factor in scleroderma patients. *Arch. Biochem. Biophys.*, **278**, 238–244.
27. Vormittag,W. and Brannath,W. (2001) As to the clastogenic-, sister-chromatid exchange inducing-and cytotoxic activity of inosine triphosphate in cultures of human peripheral lymphocytes. *Mutat. Res.*, **476**, 71–81.
28. Watrin,E. and Peters,J.M. (2006) Cohesin and DNA damage repair. *Exp. Cell Res.*, **312**, 2687–2693.
29. Uhlmann,F. (2009) A matter of choice: the establishment of sister chromatid cohesion. *EMBO Rep.*, **10**, 1095–1102.
30. Vanderheiden,B.S. (1975) ITP pyrophosphohydrolase and IDP phosphohydrolase in rat tissue. *J. Cell. Physiol.*, **86**, 167–175.
31. Vanderheiden,B.S. (1979) Inosine di- and triphosphate synthesis in erythrocytes and cell extracts. *J. Cell. Physiol.*, **99**, 287–301.
32. Sumi,S., Marinaki,A.M., Arenas,M., Fairbanks,L., Shobowale-Bakre,M., Rees,D.C., Thein,S.L., Ansari,A., Sanderson,J., De Abreu,R.A. *et al.* (2002) Genetic basis of inosine triphosphate pyrophosphohydrolase deficiency. *Hum. Genet.*, **111**, 360–367.
33. Marinaki,A.M., Duley,J.A., Arenas,M., Ansari,A., Sumi,S., Lewis,C.M., Shobowale-Bakre,M., Fairbanks,L.D. and Sanderson,J. (2004) Mutation in the ITPA gene predicts intolerance to azathioprine. *Nucleosides Nucleotides Nucleic Acids*, **23**, 1393–1397.
34. Seela,F. and Xu,K. (2007) Pyrazolo[3,4-*d*]pyrimidine ribonucleosides related to 2-aminoadenosine and isoguanosine: synthesis, deamination and tautomerism. *Org. Biomol. Chem.*, **5**, 3034–3045.

doi:10.1016/j.jmb.2010.01.027 J. Mol. Biol. (2010) 397, 179–189

JMB

Available online at www.sciencedirect.com

ScienceDirect

ELSEVIER

Structure of the Membrane Domain of Human Erythrocyte Anion Exchanger 1 Revealed by Electron Crystallography

Tomohiro Yamaguchi[1], Yohei Ikeda[1], Yoshito Abe[2], Hiroyuki Kuma[3], Dongchon Kang[4], Naotaka Hamasaki[3]* and Teruhisa Hirai[1]*

[1]*Three-Dimensional Microscopy Research Team, RIKEN SPring-8 Center, 1-1-1 Kouto, Sayo, Hyogo 679-5148, Japan*

[2]*Department of Immunology, Graduate School of Pharmaceutical Sciences, Kyushu University, 3-1-1 Maidashi, Higashi-ku, Fukuoka 812-8582, Japan*

[3]*Faculty of Pharmaceutical Sciences, Nagasaki International University, 2825-7 Huis Ten Bosch-cho, Sasebo, Nagasaki 859-3298, Japan*

[4]*Department of Clinical Chemistry and Laboratory Medicine, Graduate School of Medical Sciences, Kyushu University, 3-1-1 Maidashi, Higashi-ku, Fukuoka 812-8582, Japan*

Received 21 October 2009; received in revised form 8 January 2010; accepted 13 January 2010
Available online 25 January 2010

Edited by W. Baumeister

The membrane domain of human erythrocyte anion exchanger 1 (AE1) works as a Cl^-/HCO_3^- antiporter. This exchange is a key step for CO_2/O_2 circulation in the blood. In spite of their importance, structural information about AE1 and the AE (anion exchanger) family are still very limited. We used electron microscopy to solve the three-dimensional structure of the AE1 membrane domain, fixed in an outward-open conformation by cross-linking, at 7.5-Å resolution. A dimer of AE1 membrane domains packed in two-dimensional array showed a projection map similar to that of the prokaryotic homolog of the ClC chloride channel, a Cl^-/H^+ antiporter. In a three-dimensional map, there are V-shaped densities near the center of the dimer and slightly narrower V-shaped clusters at a greater distance from the center of the dimer. These appear to be inserted into the membrane from opposite sides. The structural motifs, two homologous pairs of helices in internal repeats of the ClC transporter (helices B+C and J+K), are well fitted to those AE1 densities after simple domain movement.

Keywords: AE1; band 3; ClC transporter; cryo-electron microscopy; two-dimensional crystal

**Corresponding authors.* N. Hamasaki is to be contacted at Faculty of Pharmaceutical Sciences, Nagasaki International University, 2825-7 Huis Ten Bosch-cho, Sasebo, Nagasaki 859-3298, Japan. T. Hirai, Three-Dimensional Microscopy Research Team, RIKEN SPring-8 Center, 1-1-1 Kouto, Sayo, Hyogo 679-5148, Japan. E-mail addresses: hamasaki-nao@niu.ac.jp; thirai@spring8.or.jp.

Present address: T. Yamaguchi, Department of Structural Biology, Graduate School of Pharmaceutical Sciences, Kyoto University, 46-29 Yoshida-Shimoadachi, Sakyo-ku, Kyoto 606-8501, Japan.

Abbreviations used: 2D, two-dimensional; 3D, three-dimensional; AE1, anion exchanger 1; AE, anion exchanger; TM, transmembrane.

Introduction

Anion exchanger 1 (AE1; also known as band 3 or SLC4A1) is the most abundant membrane protein (25% of membrane protein, 50% of integral membrane protein) in human erythrocytes.[1] AE1 consists of a 40-kDa N-terminal cytoplasmic domain (residues 1–359) and a 55-kDa C-terminal membrane domain (residues 360–911). The N-terminal hydrophilic cytoplasmic domain of AE1 serves as an anchoring point for cytoskeletal proteins, such as ankyrin,[2] protein 4.1,[3] and protein 4.2.[4] The structure of this domain has been solved by X-ray crystallography at 2.6 Å.[5] On the other hand, the membrane domain of AE1 works as a Cl^-/HCO_3^- antiporter. CO_2 produced in the tissue is converted into HCO_3^- by carbonic anhydrase II, which is bound to the C-terminus of AE1 in the red blood cell.[6] AE1 exchanges HCO_3^- with Cl^-; the "chloride shift" accomplished by this transporter lowers pH and facilitates the release of O_2 from hemoglobin. The controlled release of O_2 by sensing CO_2 ensures that tissues accept adequate levels of O_2; otherwise, tissues can be damaged by either excess or lack of O_2.[7] AE1 belongs to the anion exchanger (AE) family of electrochemical potential-driven transporters†. Members of the AE family are widespread in animals, plants, and yeast. Substrates are not limited to anions; the family includes animal bicarbonate transporters, such as the Cl^-/HCO_3^- antiporter and Na^+/HCO_3^- cotransporter,[8] and plant boron transporters.[9] AE1 transports not only Cl^- and HCO_3^- but also sulfate, phosphate, phosphoenolpyruvate, and pyridoxal 5-phosphate.[10,11] AE1 also works as a flippase.[12] The AE1 membrane domain behaves as a dimer when solubilized by detergent,[13–15] although native AE1 is known to make tetramers when ankyrin is bound to the N-terminal domain.[16]

AE1 is expressed not only in erythrocytes but also in the cells of renal collecting duct. Specific mutations of AE1 are related to such diseases as Southeast Asian ovalocytosis and distal renal tubular acidosis.[17,18] The function of AE1 is inhibited by several stilbene derivatives, such as DIDS (4,4′-diisothiocyanatostilbene-2,2′-disulfonic acid), SITS (4-acetamido-4′-isothiocyano-stilbene-2,2′-disulfonic acid), and DNDS (4,4′-dinitrostilbene-2,2′-disulfonic acid). H_2DIDS (4,4′-diisothiocyanatodihydrostilbene-2,2′-disulfonic acid)[19] can cross-link AE1 molecules almost 100%; the binding sites for the inhibitor are located at residues K539 and K851.[20] H_2DIDS binds to AE1 from the extracellular side, but the reaction sites of H_2DIDS are hidden from the cell surface when the diethyl pyrocarbonate modification takes place at His834[21] on the intracellular side of the membrane.[22] Conversely, the intracellular binding site of diethyl pyrocarbonate is hidden when H_2DIDS binds to AE1 from the extracellular side, suggesting the existence of two conformations.[22] Many biological experiments have been performed, including monoclonal antibody experiments,[23,24] *in situ* proteolytic digestion,[25,26] scanning N-glycosylation mutagenesis,[27–29] cysteine-scanning mutagenesis,[30–32] reassembly from fragments,[33,34] assessment of topogenic function,[29,35,36] and chemical modification of each type of residue (Met,[37] His,[21] Glu,[38] Tyr,[39] Arg,[40] or Lys[20,41]), to confirm the important residues and topology of AE1. From the results of these biological experiments, AE1 is expected to span the membrane up to 14 times with both the N- and C-termini on the cytoplasmic side.[32,42] Transmembrane segments 1–5 (TM1–TM5) are expected to be clustered. While co-expressed fragments TM1–TM5 + TM6–TM14 showed transport activity, any complementary pair of fragments divided between TM1 and TM5 was not active.[43] There was no tryptic cleavage site between TM2 and TM5.[26] However, the details of the protein's topology remain unclear. The 10th membrane region is thought to be very flexible because residues near K743 are observed on the external side in some experiments[27,31] and on the cytoplasmic side in others.[41,44] Although the protein has been studied for a long time, only low-resolution structures, derived from two-dimensional (2D) crystals by negative stain[45] and tubular crystal,[46] were available for the AE1 membrane domain. Here, we report 7.5-Å-resolution projection and a three-dimensional (3D) map solved by cryo-electron crystallography using a 2D crystal. This result enables us to discuss the architecture of the AE1 transporter.

We are also going to discuss the relationship between the AE1 transporter and the ClC transporter based on their structural similarity observed in this study. Members of the ClC chloride (Cl^-) channel family are widespread among prokaryotes and eukaryotes. One of the well-known functions of ClC Cl^- channels is to regulate electrical excitation in skeletal muscle.[47] The X-ray structures of a bacterial homolog of the ClC Cl^- channel were reported by Dutzler *et al.*[48,49] Interestingly, the ClC Cl^- channel homolog is shown to be a Cl^-/H^+ antiporter.[50] From the structural pseudo-2-fold symmetry, the 14 transmembrane segments of the ClC protein seem to originate from the duplication of 7 transmembrane segments. Two repeated motifs have antiparallel architecture, forming a Cl^- binding pore surrounded by several N-terminal ends of helices with conserved Cl^- binding motifs. This transporter is also inhibited by DIDS.[51] The mechanism underlying the conformational change is not known.

Results and Discussion

Structural analysis of AE1

For this study, we cross-linked AE1 with H_2DIDS in order to increase protein stability and fix the conformation into the outward-facing open form.[20,22] AE1 is crystallized two-dimensionally in a tube-like vesicle, which is about 2 μm wide and greater than 4 μm long and which seems to be flattened when applied to an electron microscopy grid (Fig. 1a). In many cases, Fourier-transformed

† http://www.tcdb.org/tcdb/

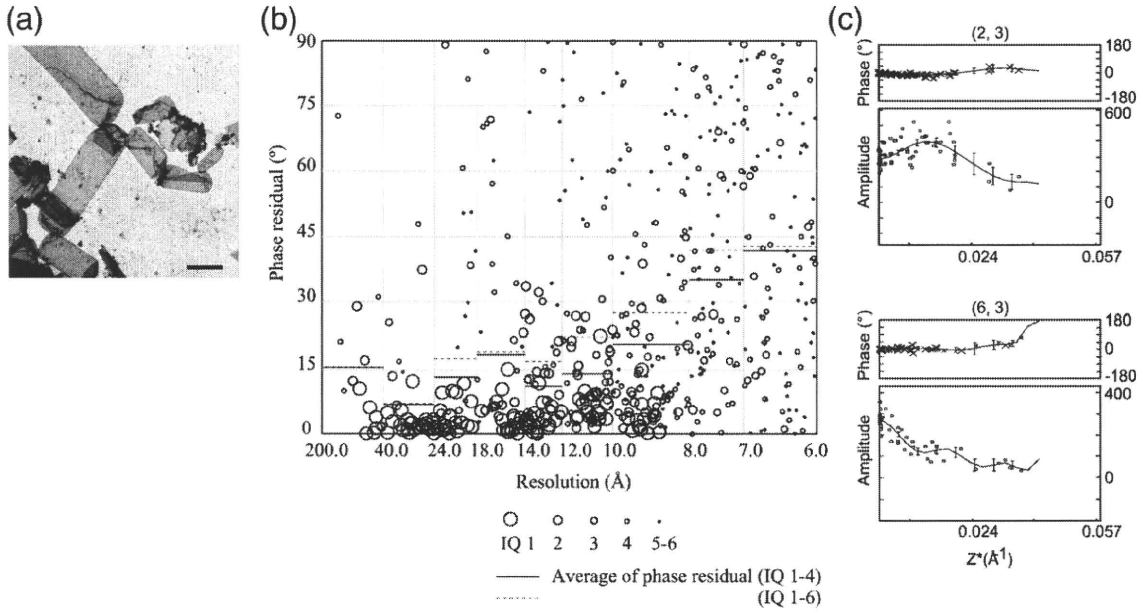

Fig. 1. Two-dimensional crystals of AE1 and the quality of processed and merged data. (a) Electron microscopy image of the negatively stained AE1 crystal. Scale bar represents 2 μm. (b) Phase deviation from either 0° or 180°. Phase deviation of averaged phases from symmetrical constraint (0° or 180°) is plotted as a function of resolution of the reflection. Averaged phase is calculated at each reflection from the four best untilted images. For this figure, IQ is defined based on the output of the *origtiltd* program from the MRC package. (c) Example of a lattice line plot. Merged data, fitted curves, and error bars of phase and amplitude information are plotted for lattice lines (2, 3) and (6, 3).

images gave two overlapping independent diffraction patterns that could be processed separately after selection by masking (Supplementary Fig. 1). The 2D plane symmetry was determined to be $p22_12_1$. Based on the deviation of phase from the symmetry requirements according to the resolution (Fig. 1b), a projection map was calculated, including data up to 7.5-Å resolution, by merging the four best images (Table 1). A 3D map of AE1 was calculated also at 7.5-Å resolution after merging 31 images tilted from 0° to 60° (7 at 0°, 8 at 20°, 12 at 45°, and 4 at 60°). Examples of lattice lines are shown in Fig. 1c and Supplementary Fig. 2a. The overall weighted phase residual was 21.4° (Table 1).

Table 1. Crystallographic data

Plane group	$p22_12_1$
Lattice constants	a=194.5 Å, b=182.0 Å, c=200 Å (assumed), $\alpha=\beta=\gamma=90°$
Resolution limit for merging (Å)	7.5
2D (projection)	
No. of images	4
Total no. of observations	2881 (IQ ≤ 6)
Completeness (%)	97.0
Overall phase error (°) from symmetrical requirement (0° or 180°)	22.5
3D	
No. of images	31 (7 at 0°, 8 at 20°, 12 at 45°, 4 at 60°)
Total no. of observations	9312 (IQ ≤ 6)
Completeness (%)	74.3 (0°–45°), 66.5 (0°–60°)
Vertical resolution (Å)[a]	16.0
Overall weighted R-factor (%)	19.4
Overall weighted phase residual (°)	21.4

[a] Estimated from point spread function (Supplementary Fig. 2b).

Projection structure of AE1

A projection map is shown in Fig. 2a. In one unit cell (194.5 Å × 182.0 Å), six dimers can be recognized. These dimers can be classified into two types: two structural homodimers (A/A) and four structural heterodimers (B/C). While the A/A dimer has a 2-fold axis in the center of dimer, molecules B and C are not crystallographically related. Half of them are upside down in the membrane, related by a screw axis parallel with the membrane. Overall, molecules A and B showed a similar density pattern, while molecule C showed a slightly dispersed density pattern. Interestingly, the projection map of the AE1 dimer (Fig. 2b) showed a pattern similar to that of the ClC transporter, which was reported by Mindell *et al.*[52] (Fig. 2c). The dimension of the rhombus shape of the dimer is ~50 Å × 100 Å in the case of the ClC transporter, while it is slightly elongated, ~50 Å × 120 Å, in the case of AE1. The density patterns for the AE1 and ClC transporters are similar, especially far from the center of the dimer, as shown in Fig. 2b and c; however, the area near the center of the dimer is less similar.

Three-dimensional structure of AE1

A 3D map of AE1 is shown in Fig. 3a–c and Supplementary Fig. 3. Horizontal sections of the

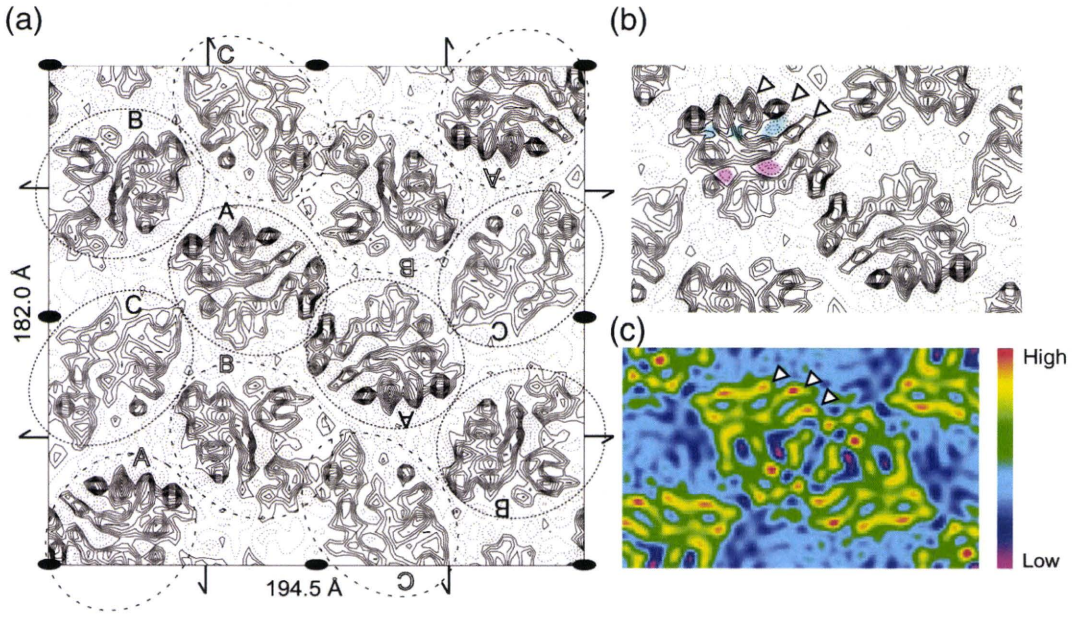

Fig. 2. Projection map of AE1 and comparison with ClC transporter. (a) Projection map of the AE1 whole unit cell (194.5 Å × 182.0 Å). Each molecule (A, B, and C) is indicated by a dotted circle to illustrate the packing. Outlined characters indicate that a molecule is upside down in the membrane (i.e., in inverted orientation compared with molecules annotated with plain characters). Two-fold axes are shown by their conventional graphic symbols. The one in the center is omitted for clarity. Arrows indicate screw axes. Contour levels are incremented by one-tenth of the maximum value. (b) Projection map of AE1 A/A dimer. (c) Projection map of ClC transporter at 6.5-Å resolution, reported by Mindell *et al.*[52] [Adapted by permission from Macmillan Publishers Ltd.: *Nature*, copyright 2001.] Several features in (b) and (c) are colored or marked to make comparison of AE1 and ClC easier. Several very low-density and low-density areas are shown in purple and blue, respectively, in (b). White arrowheads are marked in both (b) and (c) to indicate corresponding high densities.

map are also shown in Fig. 4. Even though it was not possible to count the 14 predicted transmembrane segments[32,42] in molecule A, B, or C in the map, several long and highly tilted helices were easily recognized. The longest helices spanned the membrane, running more than 50 Å in the *z*-direction at different heights, suggesting that those helices are sticking out from a membrane region (typically 40 Å wide) on different sides. In the portion of the molecule far from the center of the dimer (Fig. 3a), clustered densities are observed as an assembly of two possible helices at the V-shaped peripheral densities, along with other extra densities between or adjacent to those helices (Fig. 3b, which is presented upside down compared with Fig. 3a and c in order to allow easier comparison of the first and second V-shaped motifs). Separated by a cleft, another V-shaped density, which seems slightly rounder and wider, is recognized near the center of the dimer, without much extra density around it (Fig. 3c). Those V-shaped and wider V-shaped densities are inserted to the membrane from opposite sides (Fig. 3a). Taking the similarity in the projection map into account, helices B+C and J+K (with connecting loop) of the ClC transporter, which had similar structural features, could be fitted to the V-shaped and wider V-shaped densities, respectively. To evaluate the possibility that the extra density around the V-shaped helices (helices B+C) might correspond to helices E, F, and I, we included those helices in the model used for fitting (Fig. 3b).

Fitting structural motifs of the ClC transporter to the AE1 map

After manual fitting, positions are refined by simple domain movement, assuming two rigid bodies per molecule: one consisting of helices A+B, E, F, and I, and the other consisting of helices J+K. All models presented in Figs. 3a–c and 4 are the results of this rigid-body refinement; they fit well to the observed densities, especially considering they are derived from the different transporter family. For example, as shown in Fig. 3c, helix J is very long, but helix K is relatively short, and it ends without protruding from the membrane. Those features of the ClC model matched quite well with the 3D map of AE1. Helices B and C also fit well, though not as well as helix J+K did. Still the sharp turn made by helices B and C fits quite well to the 3D map. The density to which helix J is assigned is very fat and might include a contribution from another part of the structure (see the "+10 Å" section in Fig. 4). The density to which helix J is assigned is also connected to the large density (the upper density in Fig. 3c and the central density in the "+20 Å" section in Fig. 4) that resides on the extracellular side of membrane near the center of the dimer (2-fold axis for the A/A dimer and pseudo-2-fold axis for the B/C dimer). The longest loop, 7–8 (loop between TM7 and TM8), is on the extracellular side between the N-terminal and C-terminal halves of AE1, similar to loop I–J in the ClC protein. This unexplained density might

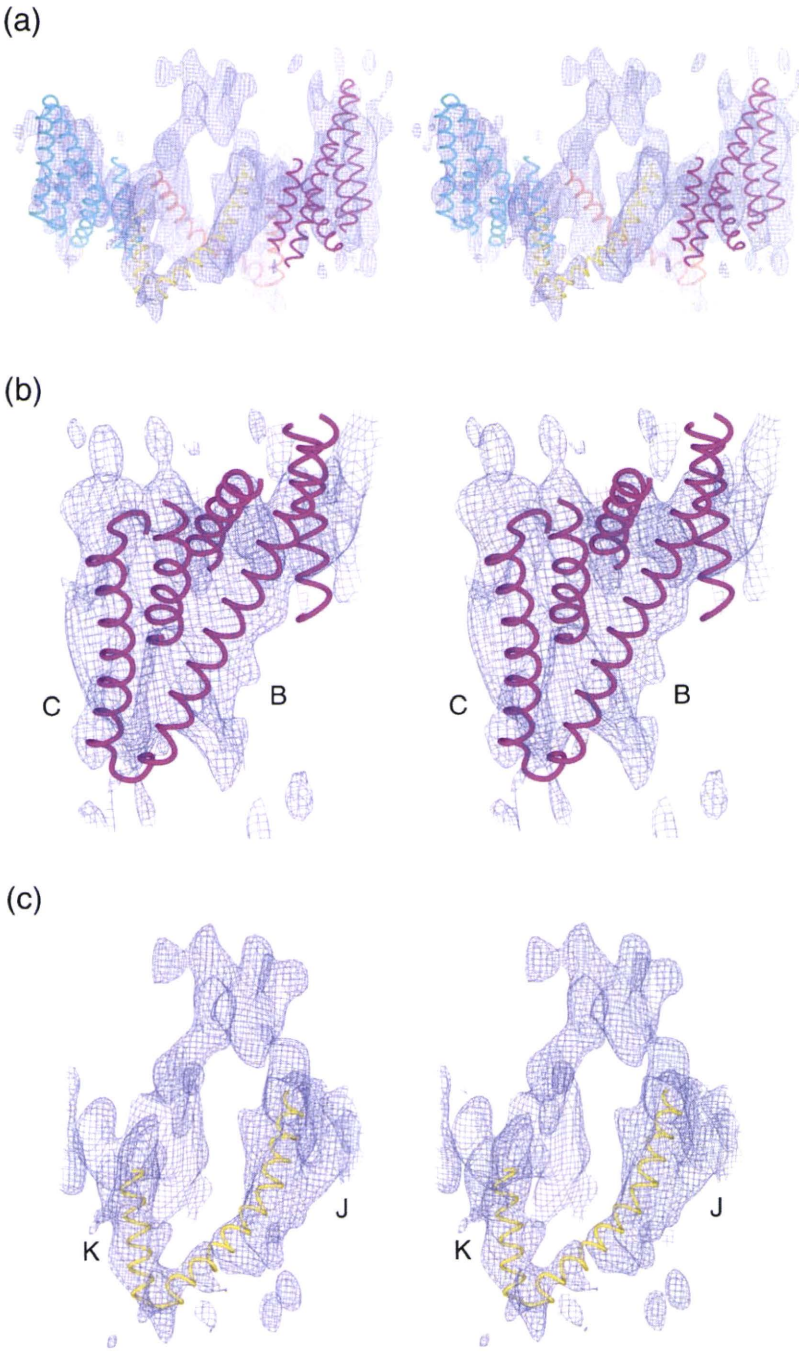

Fig. 3. Three-dimensional map of AE1 and the fitted motifs from the ClC transporter (stereo view). (a) Map of the B/C dimer with molecule B on the right side. (b) Map around the first motif (molecule B). Helices B and C in the first motif are labeled. (c) Map around the second motif (molecule C). Helices J and K in the second motif are labeled. In the case of (a) and (c), the extracellular side is up, but in the case of (b), the extracellular side is down to allow easier comparison of the first and second V-shaped motifs. The 3D map was calculated and drawn at a contour level of 1.8σ using CCP4[53] and CCP4mg.[54] All models presented in (a)–(c) are the results of rigid-body refinement. The first and second motifs of molecule B are shown in magenta and coral, respectively. The first and second motifs of molecule C are shown in cyan and yellow, respectively.

include a contribution from this central loop and/or another unmodeled part of AE1. Unexplained small density is noticeable in the vicinity of loop B–C (lower right in Fig. 3b; Supplementary Fig. 3) besides the large central density. Intra-dimeric cross-linking of single-cysteine mutants suggested that loops 1–2, 5–6, and 7–8 are close to the (pseudo-)2-fold axis,[55] although loop 1–2 is too far from the center of dimer at the current helix assignment of this conformation.

Sequence similarity between the AE family and the ClC family

Because of their structural similarity, we looked for sequence similarity between AE1 and ClC proteins. Specifically, the sequences of helices B+C of the ClC proteins are well aligned with TM1+TM2 (transmembrane helices 1+2) of the AE family, without many gaps or insertions (Fig. 5a; Supplementary Fig. 4). The sequences of helices J+K of the ClC proteins are also well aligned with those of TM8+TM9 of the AE family. To confirm the validity of the alignment between the ClC family and the AE family, we presented characteristics of the sites of the AE family on the ClC models (Fig. 5b). The charged residues clustered mainly outside of the membrane region, showing that the heights of the transmembrane segments are at least roughly aligned. The distribution of variable hydrophobic sites,[56] which normally face the lipid bilayer, seems

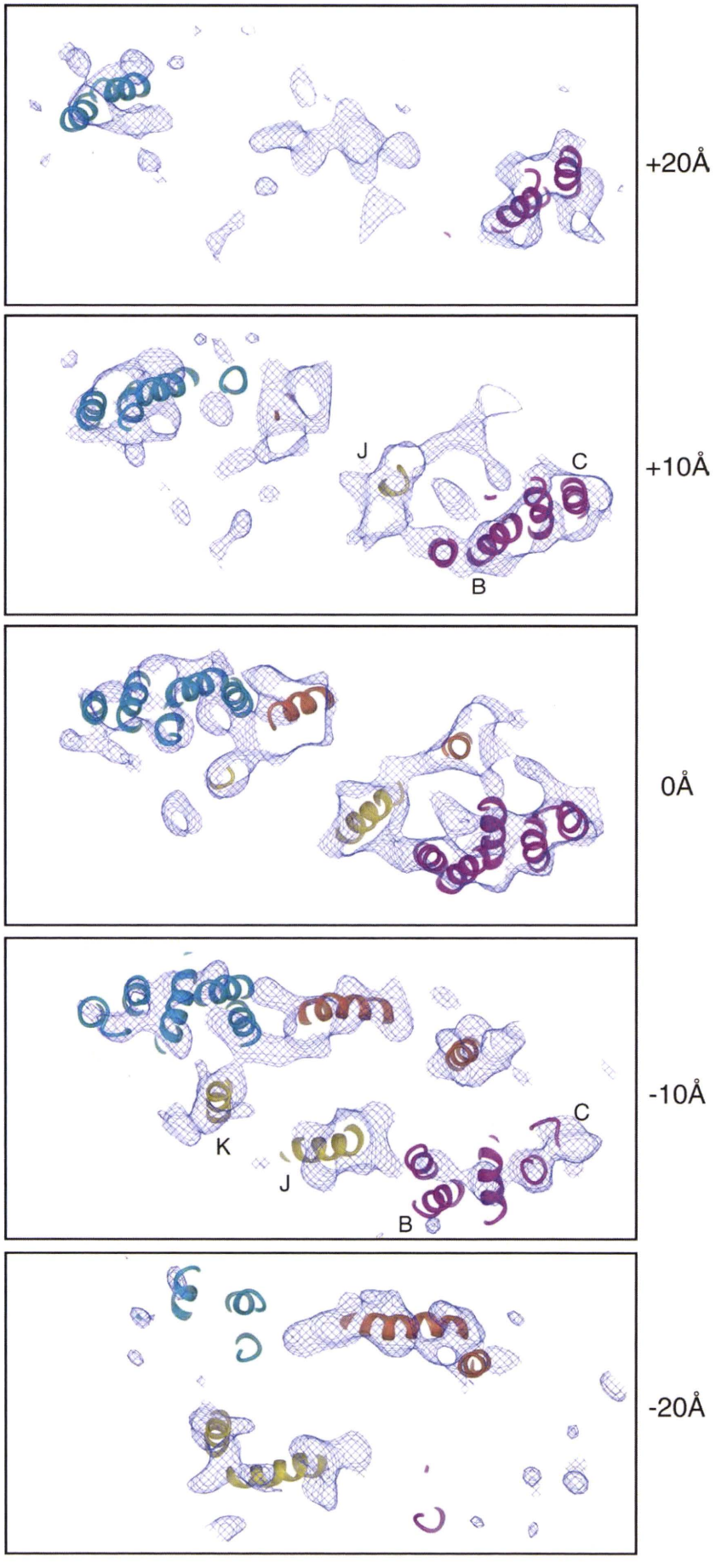

Fig. 4. Horizontal sections from the 3D map of the AE1 B/C dimer. They are sectioned at intervals of 10 Å from the center of the map, with thickness of 12 Å. Models are colored and helices are labeled as in Fig. 3.

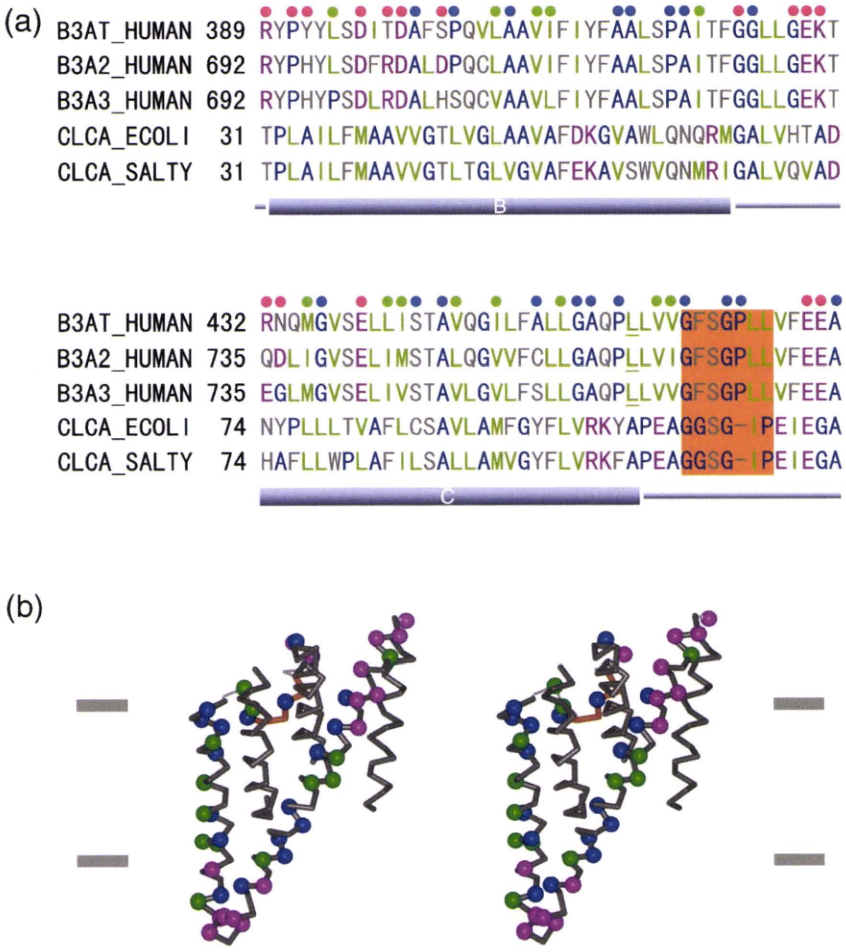

Fig. 5. Sequence alignment between the AE and ClC families. (a) Multiple sequence alignment around helices B+C of the ClC family and TM1+TM2 of the AE family and the following (putative) Cl^- binding motif. Within the presented region, the sequence identity between B3AT_HUMAN (AE1) and CLCA_ECOLI (*Escherichia coli* ClC protein) is 20%. Sites around the (putative) binding motif are highlighted in an orange box. Charged sites, variable hydrophobic sites, and small residue sites of the AE family (Materials and Methods) are marked by small filled circles shown in magenta, green, and blue, respectively. (b) Characteristics of aligned sequences of the AE family are shown on the ClC model as balls, colored as in (a) (stereo view). Possible Cl^- binding site is shown in orange. Boundaries of the membrane region, estimated based on the distribution of characteristics of residues, are indicated by horizontal bars.

to validate the rotational positioning of transmembrane segments. Small residues often appear at positions of helix–helix contact, kinks, or turns. Their distribution seems reasonable. One of the Cl^- binding sites appears soon after the end of helix C in the case of the ClC proteins. This conserved motif is represented as GSGIP, including a serine (S107) that directly contacts the Cl^- ion.[48] In the AE family, the conserved motif GXSGP, which also includes a serine (S465), is aligned at the same position; however, the density around the possible Cl^- binding site is not clear in the 3D map of AE1.

Conformational difference between the AE1 transporter and the ClC transporter

Structures of AE1 A/A and B/C dimers represented by fitted motifs are aligned and shown superposed in Fig. 6a. The second motifs (TM8+TM9) are well aligned to each other, suggesting that the dimer interface is the same between the A/A and B/C dimers. The positions of loop 1–2 (between TM1 and TM2) of molecules B and C are shifted toward the center of the dimer by 5 and 10 Å, respectively, compared with molecule A. The AE1 membrane domain is cross-linked between the N-terminal and C-terminal halves, but some structural flexibility probably still remains. Furthermore, the AE1 A/A and ClC dimers are aligned and shown superposed in Fig. 6b (top view) and c (side view). The AE1 dimer showed an elongated shape compared with the ClC dimer when it was viewed from the top (Fig. 6b). The distance between the tips of loop 1–2 of the AE1 dimer ($L1_{AE1}$) is ~110 Å, while the corresponding distance in the ClC dimer ($L1_{ClC}$) is ~90 Å. On the other hand, the width around the center of the AE1 dimer is smaller. The distance between the tips of loop 8–9 in the AE1 dimer ($L2_{AE1}$) is ~50 Å, while the corresponding distance in the ClC dimer ($L2_{ClC}$) is ~75 Å. Because of the narrower space between C-terminal halves of the AE1 dimer, the same fold that appears in the ClC molecule is not possible for the C-terminal half of AE1 (after the second motif) in the current structure. The displacement of height between the tips of loop 1–2 and loop 8–9 is ~60 Å for AE1 ($H1_{AE1}$), while the corresponding distance is ~40 Å for ClC proteins ($H1_{ClC}$), resulting in a larger protrusion from the membrane regions of AE1.

Conclusions

Based on the structural and sequence homology between AE1 and ClC proteins in the regions of the

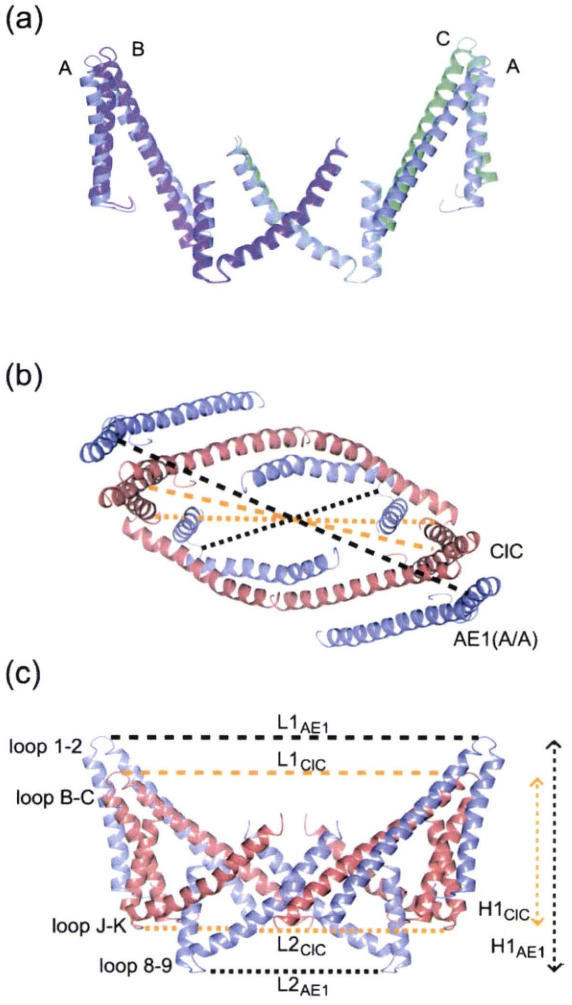

Fig. 6. Comparison between the AE1 A/A dimer, AE1 B/C dimer, and ClC dimer. (a) Superposition of the AE1 A/A and B/C dimers. Molecules A, B, and C are shown in purple, magenta, and cyan, respectively. (b and c) Comparison of the AE1 A/A and ClC dimers (b, top view; c, side view). The AE1 and ClC dimers are shown in purple and coral, respectively. For this figure, only the first and second motifs are shown. The A/A dimer in (a) is rotated 30° along the *z*-axis, compared with the A/A dimer in (c).

two-helix repeated motifs (TM1+TM2 and TM8+TM9 of AE1 and helices B+C and J+K of ClC proteins), we presume that the two protein families share the same antiparallel structural framework, although it remains unknown as to what extent they share a transport mechanism. Because both AE1 and ClC proteins share the same asymmetry between the first and second motifs, it is most likely that they diverged after that asymmetry appeared in the common ancestor. However, the present 3D map does not give detailed information, especially in the region following the second motif, and sequence similarity is also very weak in that region. As discussed, the C-terminal half of AE1 in the current conformation will have a different fold compared with the reported structure of the ClC transporter after the second motif. The region around TM10 is known to be very flexible based on the accessibility of K743 from both sides of the membrane. TM10 also has a very hydrophilic character, and it can be easily released by *in situ* proteolytic digestion after alkali treatment (10 mM NaOH, pH 12). (The regions released only after alkali treatment are called "category 2".[25]) An analysis of topogenic functions shows that TM10 itself does not have any topogenic function.[35] This kind of flexibility could be one of the reasons why the map does not show a clear density around that region.

Although the AE1 and ClC transporters have structural similarity, their conformations are significantly different. It is not yet known whether this reflects a family-wide difference or rather represents a conformational change in the chloride transporter. Further investigation is necessary to understand the transport mechanism of AE1 and to determine the significance of the similarity between AE1 and ClC transporters.

Materials and Methods

Purification of AE1

Human blood stored at 4 °C in acid/citrate/dextrose solution was obtained from the Fukuoka Red Cross Blood Center. Erythrocyte membranes (white ghosts) were prepared as described previously.[57] White ghosts (~400 mg) were incubated with H_2DIDS (2 mg, Molecular Probes) in 10 mM borate buffer (pH 9.5) at 37 °C for 90 min. To remove the N-terminal cytoplasmic domain of AE1, we treated the membranes with TPCK (L-1-tosylamido-2-phenylethyl choloromethyl ketone)-trypsin (0.4 mg, Roche Diagnostics) in 5 mM Na_2CO_3 for 30 min on ice. Peripheral membrane proteins were stripped by 10 mM NaOH. Membrane proteins were solubilized with 0.1% (v/v) $C_{12}E_8$ (Wako) and deglycosylated with *N*-glycosidase F (100 U, Roche Diagnostics) simultaneously for 24 h at room temperature. Solubilized AE1 was then purified using POROS HQ/20 anion exchange column (Applied Biosystems) by HPLC (BioCAD 700E perfusion chromatography). Purified AE1 was concentrated by the batch method with DEAE Sepharose resin (GE Healthcare). In this step, the detergent $C_{12}E_8$ was exchanged with $C_{13}E_8$.

Two-dimensional crystallization

After mixing solubilized protein and lipid, we performed 2D crystallization of AE1 by removing detergent using button dialysis. The protein was mixed with DOPS (1,2-dioleoyl-*sn*-glycero-3-phospho-L-serine, SIGMA) at 2.5 mg protein/ml at a lipid-to-protein-ratio of 0.14–0.16 (w/w) in 0.09% (v/v) $C_{13}E_8$ (Anatrace) and 0.01% (v/v) $C_{12}E_8$, and dialysis was performed in a dialysis button, initially against 10 mM Tris, pH 8.0, 100 mM NaCl, and 0.02% NaN_3 at 26 °C for 8 days and then against 10 mM Tris, pH 8.0, 20 mM NaCl, 10 mM $Na_4P_2O_7$, and 0.02% NaN_3 at 26 °C for 5 days. For screening of 2D crystallization conditions, samples were negatively stained with 2% (w/v) uranyl acetate on glow-discharged carbon-coated Cu grids and then observed using a JEOL